universität wien

BACHELOR'S THESIS

Title of the Bachelor's Thesis

"Propagating spin wave spectroscopy in surface, backward volume and forward volume geometries"

submitted by

Mag. arch. Iva Simonovic

in partial fulfillment of the requirements for the degree of

Bachelor of Science (BSc)

Vienna, 2025

degree programme code as it appears on the student record sheet:	A 033 676
degree programme as it appears on the student record sheet:	Bachelorstudium Physik
Supervisor:	Univ.-Prof. Dr. Andrii Chumak

Acknowledgments

I would like to sincerely thank Prof. Andrii Chumak and the entire NANOMAG Group for their warm welcome and support.

Also, I am grateful to Khrystyna Levchenko, Ph.D., for her invaluable guidance, enthusiasm, and willingness to help with any endeavor.

A special thank you goes to Kristýna Davídková, M.Eng., for her continuous, amazing and patient support, insightful advice and encouragement, as well as for always being available to answer any questions, whether simple or complex.

Contents

Abstract

Magnetism is a cornerstone of modern technology, driving advancements in data storage, wireless communication, and electronic devices. In recent years, the field of magnonics, which explores spin waves, the collective excitations in magnetic materials, has gained increasing attention. Spin waves offer a promising alternative to conventional charge-based electronics for information transport and processing, as they enable signal propagation without the movement of electrical charges and thus, significantly reducing energy dissipation.

This thesis describes the fundamental principles of magnetization dynamics, with a particular focus on spin waves. It also examines key experimental techniques used to study these phenomena, specifically Ferromagnetic Resonance (FMR) and Propagating Spin Wave Spectroscopy (PSWS). The experiments were conducted for different modes of spin waves using a Vector Network Analyzer (VNA). FMR and PSWS measurements on Yttrium-Iron-Garnet (YIG) were conducted to establish a fundamental understanding of measurement techniques.

Given the importance of PSWS in investigating spin wave dynamics, this work contributes to the field by developing a novel sample holder that enables not only measurements in in-plane configurations, but also introduces the capability for out-of-plane measurements. This new design enhances research capabilities and expands experimental possibilities at the University of Vienna.

The effectiveness of the new setup was validated through PSWS experiments on YIG, demonstrating its potential for future studies in magnonic research.

Motivation

Magnetism plays a crucial role in modern technology, enabling innovations in data storage, wireless communication, and sensing applications. As research in this field progresses, alternative approaches to conventional electron-based electronics are being explored.

One promising approach is in the field of magnonics, which focuses on the study of spin waves, the collective excitations of magnetization in magnetic materials. Magnons, the quasi particles or quanta of spin waves, give the field its name. Due to the unique properties of spin waves, such as their ability to transfer information with significantly lower energy dissipation compared to conventional charge-based electronics, spin wave-based devices have the potential to outperform conventional electronic systems in terms of both energy efficiency and footprint. The research field aims to develop innovative devices for information technology and microwave signal processing. Spin waves can reach frequencies in the range of THz, making them highly promising for next-generation telecommunications (e.g., 5G and beyond). Additionally, their nano-scale wavelength allows for device miniaturization, making them especially suitable for advanced nano-scale information processing technologies [1], [2].

However, accurately characterizing spin wave dynamics remains a challenge and requires precise experimental techniques to explore different propagation modes and material properties. Two useful methods are Ferromagnetic Resonance (FMR) and Propagating Spin Wave Spectroscopy (PSWS). FMR provides fundamental insights into magnetic damping and material properties, while PSWS enables direct investigation of propagating spin waves. These techniques, as described in this thesis, are crucial methods for gaining insights into the dynamics of spin waves in ferromagnetic materials, for example Yttrium Iron Garnet (YIG), a widely used material in magnonic research due to its low damping and excellent spin wave properties, even referred to as 'miracle material' ([3]).

To enhance the research capabilities at the University of Vienna, a very important aspect of this thesis was the development of a novel sample holder that enables an additional mode of measurement. The original setup provided the measurement in two in-plane configurations, where a thin film of a magnetic material is placed parallel to the direction of the magnetic field of an electromagnet. In one configuration, spin waves are excited to propagate parallel to the magnetic field, this mode is called Backward Volume Spin Waves (BV). In the other configuration, the spin waves propagate perpendicular to the direction

of the magnetic field, referred to as the Damon-Eshbach Magnetostatic Spin Waves (DE). The newly designed sample holder expands the setup to support both in-plane and out-of-plane spin wave propagation modes, significantly broadening the range of possible experiments. In the out-of-plane configuration, the magnetic thin film is oriented perpendicular to the direction of the magnetic field, and the spin waves are excited to propagate perpendicular to the magnetic field, this mode is referred to as Forward Volume Magnetostatic Spin Waves (FV).

Thesis Structure:

The **first chapter** provides the fundamental concepts of magnetism and magnetization dynamics, along with an overview of the underlying theoretical framework.

The **second chapter** explores spin waves in greater detail, discussing their various propagation modes and the corresponding dispersion relations, which are crucial in dealing with spin wave dynamics.

The **third chapter** presents a brief overview of Yttrium Iron Garnet (YIG) as a key material in spin wave research.

The **fourth chapter** introduces the Vector Network Analyzer (VNA) and explains the importance of scattering parameters in analyzing spin wave transmission.

The **fifth chapter** details the experimental procedure and analysis of Ferromagnetic Resonance (FMR) in YIG, including the extraction of interesting parameters such as the damping parameter, inhomogeneous linewidth broadening, and saturation magnetization.

The **sixth chapter** focuses on propagating spin wave spectroscopy (PSWS), and explains the development of the new sample holder for out-of-plane measurements, and the experimental results obtained using the enhanced laboratory setup.

Finally, the **Conclusion** summarizes the findings.

1 Theoretical Background

This chapter provides a brief overview of the fundamental concepts of magnetism and magnetic materials. It introduces different types of magnetic fields, including applied and internal magnetic fields, to establish a foundation for understanding the micromagnetic energy contributions to the effective magnetic field. The discussion then extends to the dynamics of magnetic materials, laying the groundwork for the explanation of spin waves and their behavior in the following chapter. This chapter is based mainly on the books [4] and [5].

1.1 Introduction to Magnetism

The magnetic moment in a magnetic material is created by an electron in orbital motion around the nucleus of an atom. Since an electron is a charged particle, when it moves around the nucleus, it can be also seen as a current loop, which induces the magnetic moment $\boldsymbol{\mu}_\mathrm{L} = -\frac{e}{2m_\mathrm{e}}\boldsymbol{L}$.

The gyromagnetic ratio γ is the constant of proportionality between the angular momentum and the magnetic moment $\boldsymbol{\mu}_\mathrm{L} = \gamma\boldsymbol{L}$. This shows that when the angular moment changes, the magnetic moment changes and vice versa. Because the electron is negatively charged, $\boldsymbol{\mu}_\mathrm{L}$ and $\boldsymbol{L}$ are antiparallel.

Additionally, the electron has an intrinsic angular momentum called spin, which can be described by $\boldsymbol{\mu}_\mathrm{S} = -\frac{e}{m_\mathrm{e}}\boldsymbol{S}$. The spin, though it is a quantum mechanical quantity, generates a magnetic field that can be interpreted as a magnetic dipole from a certain distance. When exposed to an external magnetic field $\boldsymbol{B}$ the spin experiences the torque $\boldsymbol{\tau} = \boldsymbol{\mu}_\mathrm{S} \times \boldsymbol{B}$ [4, p. 80].

The total magnetic moment is then defined as the sum of the classical and the quantum mechanical angular momenta as in eq.(1).

$$\boldsymbol{\mu} = \boldsymbol{\mu}_\mathrm{L} + \boldsymbol{\mu}_\mathrm{S} = -\frac{e}{2m_\mathrm{e}}(2\boldsymbol{S} + \boldsymbol{L}) \tag{1}$$

μ ... magnetic moment

μ_L ... classical angular momentum

μ_S ... quantum mechanical momentum

e ... charge of electron

m_e ... mass of electron

$\boldsymbol{S}$ ... vector sum of the spin angular momenta of all electrons in an atom

$\boldsymbol{L}$ ... vector sum of the angular momenta of all electrons in an atom

The vector sum of all magnetic moments $\boldsymbol{\mu}_\mathrm{i}$ in the magnetic material per volume is called magnetization $\boldsymbol{M} = \sum_i \frac{\boldsymbol{\mu}_i}{V}$. The saturation magnetization M_S is the maximum value of M and occurs, when all magnetic moments are aligned in the same direction when subjected to an external magnetic field. The saturation magnetization varies across different magnetic materials, depending on factors such as the crystal structure and material-specific properties [4, p. 24].

An important value of magnetic materials is the susceptibility $\chi = \frac{\boldsymbol{M}}{\boldsymbol{H}}$, which shows that in linear materials the relation between the magnetization and the magnetic field is also linear. The susceptibility reveals how a material behaves in an external magnetic field, caused by the different values of the magnetic moments, that is, their magnitudes and alignments. Depending on the value of χ, magnetic materials are classified as: dia-, para-, ferro-, ferri- and antiferromagnetic.

It is also necessary to clarify the relation between the magnetic field strength $\boldsymbol{H}$ and the magnetic flux density or magnetic inductance $\boldsymbol{B}$ (which is also often called magnetic field). The flux density in vacuum outside of the magnetic sample is simply defined as $\boldsymbol{B} = \mu_0 \boldsymbol{H}$, with the vacuum permeability $\mu_0 = 1.257 \times 10^{-6} N/A^2$. But inside of a magnetic structure it changes to $\boldsymbol{B}_\mathrm{int} = \mu_0(\boldsymbol{H}_\mathrm{int} + \boldsymbol{M})$, which includes the magnetization. The internal magnetic field $\boldsymbol{H}_\mathrm{int}$ experienced by a magnetic moment consists of two components: $\boldsymbol{H}_\mathrm{int} = \boldsymbol{H}_\mathrm{ext} + \boldsymbol{H}_\mathrm{d}$. The first component is the external applied field $\boldsymbol{H}_\mathrm{ext}$ and depends on the shape of the sample. For example, for a thin film placed in an in-plane magnetic magnetic field the external field $\boldsymbol{H}_\mathrm{ext}$ looks like this:

$$\boldsymbol{H}_\mathrm{ext} = \frac{\boldsymbol{B}_\mathrm{ext}}{\mu_0} \tag{2}$$

For a saturated thin film positioned perpendicular (out-of-plane) to the applied magnetic field the external field looks like this:

$$\boldsymbol{H}_\mathrm{ext} = \frac{\boldsymbol{B}_\mathrm{ext}}{\mu_0} - \boldsymbol{M}_\mathrm{S} \tag{3}$$

The other component is the demagnetization field $\boldsymbol{H}_\mathrm{d}$ which is directed in the opposite direction of the magnetization, so antiparallel. It is caused by uncompensated magnetic

moments at the surface of a magnetic material, which then appears to have opposite magnetic poles and depends mainly on the geometry of the sample and the saturation magnetization M_S of the material [4, p. 480]. The demagnetization field $\boldsymbol{H}_d$ is defined as [6, p. 36]:

$$\boldsymbol{H}_d = -\overline{\boldsymbol{N}} \cdot \boldsymbol{M} \tag{4}$$

where $\overline{\boldsymbol{N}}$ (eq.5) is the symmetric demagnetizing tensor with unit trace $tr(\overline{\boldsymbol{N}}) = 1$ [5, p. 150]. The diagonal elements are called demagnetizing factors, which contain the geometry of the sample .

$$\overline{\boldsymbol{N}} = \begin{pmatrix} N_{xx} & 0 & 0 \\ 0 & N_{yy} & 0 \\ 0 & 0 & N_{zz} \end{pmatrix} \tag{5}$$

For example, for a thin film placed in the xy-plane parallel to the magnetic field, the parallel-aligned demagnetizing factors are equal to zero, and only the matrix component N_{zz}, which is perpendicular to the magnetic field, is equal to 1 (in SI units). In contrast, for a sphere, where the diagonal elements can be magnetized in any direction due to isotropy, all demagnetizing factors are equal, so $N_{xx} = N_{yy} = N_{zz} = 1/3$ (in SI units) [4, p. 32], [7, p. 25].

1.2 Micromagnetic Energies

To describe magnetization dynamics, it is necessary to explain the micromagnetic energies contributing to the effective magnetic field $\boldsymbol{H}_{eff}$ which is acting on a magnetic system. Magnetic systems are inclined to minimize their energy state. These energies and the related fields are described by the theory of micromagnetism in mesoscopic dimensions. Mesoscopic means, the theory contains the microscopic dimensions of quantum mechanics and the macroscopic dimensions of Maxwell's theory. The most significant contributing energies are: dipolar energy E_d, exchange energy E_{ex}, Zeeman energy E_Z and anisotropy energy E_a.

The **dipolar energy** E_d, also referred to as magnetostatic energy, arises from the weak, long-ranged dipole-dipole interaction between magnetic moments, expressed as eq.(6) [4,

p. 37 and p. 348]. It is related to the before mentioned demagnetization field $\boldsymbol{H}_\mathrm{d}$ within the material and thus also depends on the shape of the sample.

$$E_\mathrm{d} = -\frac{1}{2}\mu_0 \int_V \boldsymbol{H}_\mathrm{d} \cdot \boldsymbol{M} \mathrm{dV} = -\frac{1}{2}\mu_0 \int_V (-\overline{N} \cdot \boldsymbol{M}) \cdot \boldsymbol{M} \mathrm{dV} \tag{6}$$

The minimum dipolar energy is reached, when the moments are aligned antiparallel.

The **exchange energy** E_ex comes from the quantum mechanical coupling interaction between two neighboring spins S_i, S_j in units of $\hbar$ due to Coulomb repulsion and it is short-distance and strong. It also explains the origin of the Weiss internal field of ferromagnets [4, p. 102].

$$E_\mathrm{ex} = E_\mathrm{ij}^{exch} = -2J_\mathrm{ij}\boldsymbol{S}_\mathrm{i} \cdot \boldsymbol{S}_\mathrm{j} \tag{7}$$

J_ij is the exchange integral between two atoms i and j, and shows the alignment of the two spins. If $J_\mathrm{ij} < 0$, E_ex reaches minimum for antiparallel spins, which shows antiferromagnetic order and if $J_\mathrm{ij} > 0$, E_ex is minimal for parallel spins in ferromagnetic order [4, p. 102].

The **Zeeman energy** E_Z results from the interaction of the external magnetic field $\boldsymbol{H}_\mathrm{ext}$ with the magnetization $\boldsymbol{M}$, and it reaches its minimum, when all magnetic moments are aligned parallel to the applied external field. It is described by the following equation:

$$E_\mathrm{Z} = -\mu_0 \int_V \boldsymbol{M} \cdot \boldsymbol{H}_\mathrm{ext} \mathrm{dV} \tag{8}$$

This expression is directly related to the potential energy $U = -\mu_0 \boldsymbol{m} \cdot \boldsymbol{B}_\mathrm{ext}$ acting on the magnetic moment $\boldsymbol{m}$ in the external applied field $\boldsymbol{B}_\mathrm{ext}$ [4, p. 282].

And finally, the **anisotropy energy** E_a is derived from the crystal lattice configuration in a material and depends on the orientation of the crystal lattice. In symmetrical lattices, the magnetization aligns along a preferred axis to minimize energy. The anisotropy energy depends on the angle Θ between the magnetization and the preferred axis in the crystal lattice, reaching a minimum when they are perfectly aligned. The simplest case, e.g., uniaxial anisotropy with only one preferential axis, is given by (eq.(9)):

$$E_\mathrm{a} = \int_V K_\mathrm{u} sin\Theta^2 \mathrm{dV} \tag{9}$$

where K_u is the anisotropy constant (energy density), which characterizes the crystal lattice [4, p. 271].

The total energy is the sum of all energies:

$$E = E_{\mathrm{d}} + E_{\mathrm{ex}} + E_{\mathrm{Z}} + E_{\mathrm{a}} \tag{10}$$

Eventually, the sum of the magnetic fields derived from the micromagnetic energies describe the effective field $\boldsymbol{H}_{\mathrm{eff}}$:

$$\boldsymbol{H}_{\mathrm{eff}} = \boldsymbol{H}_{\mathrm{d}} + \boldsymbol{H}_{\mathrm{ex}} + \boldsymbol{H}_{\mathrm{Z}} + \boldsymbol{H}_{\mathrm{a}} \tag{11}$$

So, when the magnetization is aligned along the direction of the effective field, this is the state of minimal energy, which is called the steady state. But when the magnetization deviates from the preferred direction, torque $\boldsymbol{T}$ arises due to the influence of the effective field, causing the magnetization to precess [4, p. 9].

$$\boldsymbol{T} = \mu_0 \boldsymbol{M} \times \boldsymbol{H}_{\mathrm{eff}} \tag{12}$$

1.3 Dynamics of Magnetization

The above described process of the alignment of the magnetization along the direction of the magnetic field, can also be viewed from an individual magnetic moment $\boldsymbol{m}$. When it is exposed to an external magnetic field H_{eff}, it will align with that field, which is exactly the pursued state of minimum energy.

The equation of motion for the steady state:

$$\frac{\partial \boldsymbol{M}}{\partial t} = 0 \tag{13}$$

Now if there is another smaller magnetic field $h_{\mathrm{ext}}(t)$ applied, which has a differing direction relative to $\boldsymbol{H}_{\mathrm{eff}}$, ideally perpendicular to $\boldsymbol{H}_{\mathrm{eff}}$, the magnetic moment will experience a torque $\boldsymbol{T} = \mu_0(\boldsymbol{m} \times \boldsymbol{H}_{\mathrm{eff}})$ caused by the magnetic field $\boldsymbol{H}_{\mathrm{eff}}$. This leads to the precession of the magnetic moment around the steady state, as explained before.

The magnetization precession with the Larmor Frequency $\omega = \gamma \mu_0 H_{\mathrm{eff}}$ is described by the Landau-Lifshitz equation (LL-eq.) [7, p. 33]:

$$\frac{\partial \boldsymbol{M}}{\partial t} = -\gamma \mu_0 (\boldsymbol{M} \times \boldsymbol{H}_{\mathrm{eff}}) \tag{14}$$

Generally, the LL-eq. describes the ideal situation without energy dissipation, but in reality the precession is dampened depending on the material and this is considered by

introducing the Gilbert damping parameter α. The LL-eq. is expanded into by the Landau-Lifshitz-Gilbert equation (LLG-eq.) (eq.15) (taken from [7, p. 33]).

$$\frac{\partial \boldsymbol{M}}{\partial t} = -\gamma\mu_0(\boldsymbol{M} \times \boldsymbol{H}_{\text{eff}}) + \frac{\alpha}{M_{\text{S}}}(\boldsymbol{M} \times \frac{\partial \boldsymbol{M}}{\partial t}) \tag{15}$$

$\boldsymbol{M}$ ... magnetization [A/m]

t ... time

γ ... gyromagnetic ratio, $\gamma = 28 \cdot 2\pi \cdot 10^9 rad/(s \cdot T)$

μ_0 ... vacuum permeability, $\mu_0 = 1.257 \times 10^{-6} N/A^2$

$\boldsymbol{H}_{\text{eff}}$ ... effective magnetic field [A/m]

α ... Gilbert damping parameter, unit-less

M_{S} ... saturation magnetization [A/m]

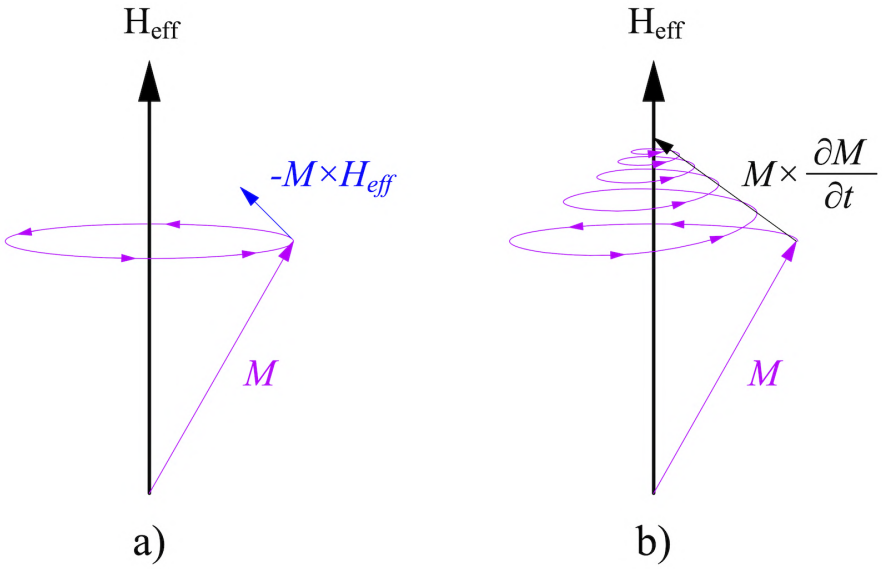

Figure 1: Illustration of the precession of magnetization M around H_{eff}. Precession in a) is described by the LL-eq.(14) without damping (blue arrow) and in b) with damping (small black arrow) and hence the motion is described by the LLG-eq.(15).

2 Spin Dynamics

In the following, the dynamic behavior of spins in magnetic materials is discussed. The chapter begins with the simplest case of spin dynamics, uniform spin precession, namely Ferromagnetic Resonance, where all magnetic moments precess in phase under the influence of an external magnetic field. Next, propagating spin waves are introduced, with a focus on their fundamental properties. An essential feature of spin wave behavior is the dispersion relation, which describes how the spin wave frequency depends on the wave vector. This relation is strongly influenced by the geometric configuration of a magnetic sample, relative to the applied magnetic field. We will focus on examining thin magnetic films. The chapter then delves into higher-order spin wave modes, such as perpendicular standing spin waves, discussing the boundary conditions for pinned and unpinned modes. Finally, the Kalinikos-Slavin model is presented to describe the spin wave dispersion in thin films. The primary sources used in writing this chapter are [5] and [7].

2.1 Ferromagnetic Resonance

We now focus on the simplest case of spin dynamics, the **Ferromagnetic Resonance** (FMR), a phenomenon that occurs when the precessions of all magnetic moments in a thin magnetic sample are in phase, leading to non-propagating spin waves with a wave vector of $\boldsymbol{k} = 0$. This resonance condition provides valuable insight into the dynamics of magnetization in magnetic materials.

Furthermore, FMR occurs, when the angular precession frequency of the magnetization in a magnetic material coincides with the frequency of the applied oscillating magnetic field, $\boldsymbol{b}_{\text{ext}}(t)$, which is induced by microwaves from an AC current. In other words, the precession frequency of the magnetization has a maximum, when the applied frequency is equal to the eigen-frequency of the magnetic material. This coincides with the maximum absorption of energy in a magnetic sample, that is why in the graph of FMR measurement (Fig.2) this is actually displayed as a minimum.

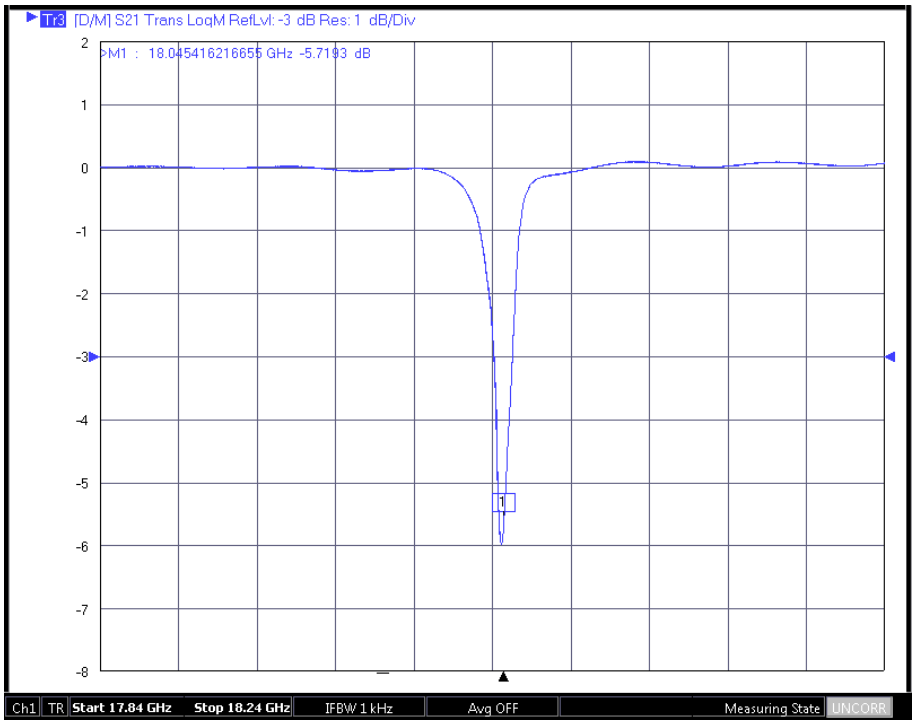

Figure 2: Example graph for FMR measurement with a Vector Network Analyzer of a Yttrium-Iron-Garnet thin film (d = 100 nm) at B = 550 mT. The spectrum shows the transmission minimum, corresponding to the maximum energy absorbed. (source: measured during the Nanotechnology Labcourse)

The FMR condition depends on the material itself, e.g., on the orientation of the magnetic material relative to the magnetic field, and the dimensions of the sample. This is obvious, when the following equations (16 - 18) (in SI units) for the resonance frequencies of different shapes of samples are regarded ([7, p. 25], [8]).

for a sphere (Larmor frequency):

$$\omega_{\mathrm{L}} = \gamma B_{\mathrm{ext}} \tag{16}$$

for a thin film out-of-plane, perpendicular to the magnetic field:

$$\omega = \gamma(B_{\mathrm{ext}} - \mu_0 M_{\mathrm{S}}) \tag{17}$$

for a thin film in-plane, parallel to the magnetic field (Kittel formula):

$$\omega = \gamma\sqrt{B_{\mathrm{ext}}(B_{\mathrm{ext}} - \mu_0 M_{\mathrm{S}})} \tag{18}$$

These equations are derived as solutions in limiting cases of an ellipsoid for the Landau-Lifshitz eq.(14) with the effective field only depending on the dipolar field, which in itself

depends on the dimensions on the sample and the applied external field: $\boldsymbol{H}_{\text{eff}} = \boldsymbol{H}_{\text{d}} + \boldsymbol{H}_{\text{ex}}$. Since the magnetization $\boldsymbol{M}$ is aligned with $\boldsymbol{H}_{\text{eff}}$, and saturation magnetization is achieved, $\boldsymbol{M}$ can be replaced with saturation magnetization M_{S}.

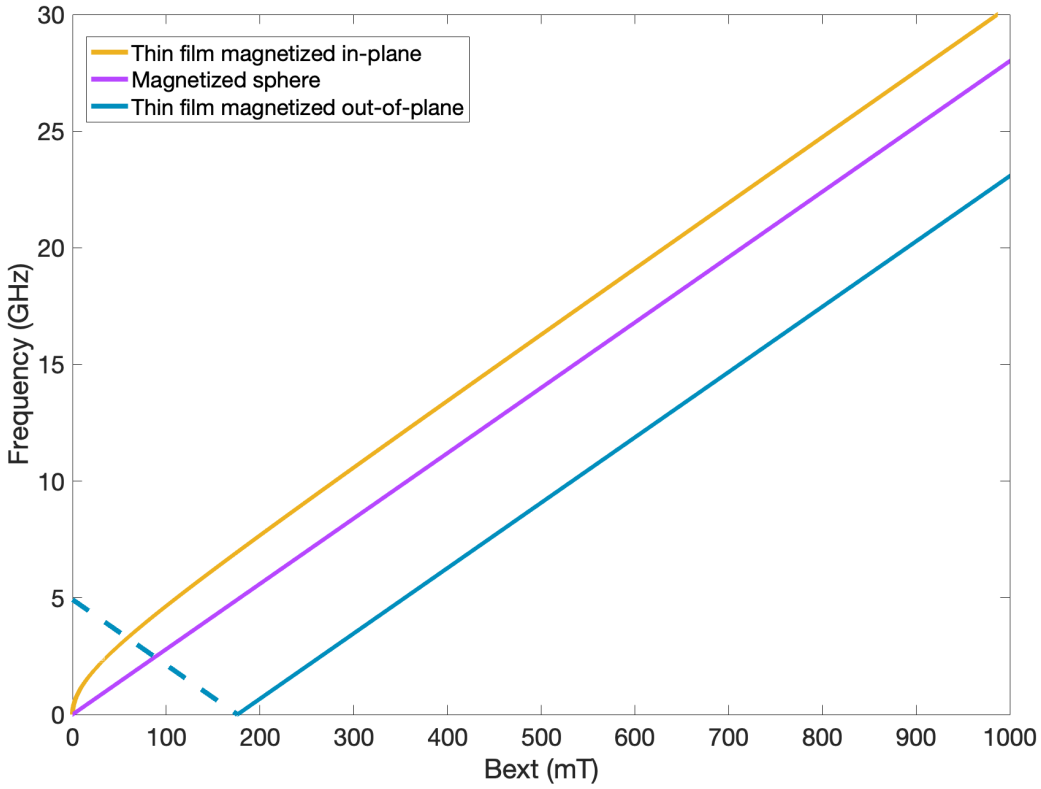

Figure 3: This figure shows the resonant frequencies as a function of the applied field B_{ext} for different sample geometries and magnetization configurations: a sphere (purple line), a thin film magnetized in-plane (IP) (yellow line), and a thin film magnetized out-of-plane (OOP) (blue line). The curves exhibit distinct behaviors due to the influence of the magnetic fields. The sphere has a linear dependence (Larmor frequency), while the OOP configuration shows a shifted linear relation due to the subtraction of the demagnetizing field term $\mu_0 M_{\text{S}}$. In contrast, the IP thin film follows a square root dependence (Kittel formula), resulting in a non-linear curve that initially grows rapidly. The dashed segment of the OOP curve corresponds to a non-physical regime where represents where $B_{\text{ext}} < \mu_0 M_{\text{S}}$ meaning spin waves cannot be excited or observed experimentally. These differences highlight the influence of internal magnetic interactions and boundary conditions on the spin dynamics due to different geometries [8].

We are further focusing on two important instances of linear FMR, which are thin films

arranged either in-plane (IP) or out-of-plane (OOP) with respect to the external field. The internal magnetic field strength is defined for a fully saturated thin film in IP configuration $\boldsymbol{H}_{\text{int,IP}} = \frac{\boldsymbol{B}_{\text{ext}}}{\mu_0}$ depending on the external field $\boldsymbol{B}_{\text{ext}}$ and separately for the OOP configuration $\boldsymbol{H}_{\text{int,OOP}} = \frac{\boldsymbol{B}_{\text{ext}}}{\mu_0} - \boldsymbol{M}_{\text{S}}$, with the saturation magnetization M_{S}. Then the resonant frequencies in terms of the angular frequencies ω_{H} and ω_{M} for these two cases are as follows [7, p. 24]:

$$\omega_{\text{FRM,IP}} = \omega_{\text{H}} \tag{19}$$

$$\omega_{\text{FRM,OOP}} = \sqrt{\omega_{\text{H}}(\omega_{\text{H}} + \omega_{\text{M}})} \tag{20}$$

where ω_{H} and ω_{M} are defined as:

$$\omega_{\text{H}} = \gamma\mu_0 H_{\text{int}} \tag{21}$$

$$\omega_{\text{M}} = \gamma\mu_0 M_{\text{S}} \tag{22}$$

When the deflection angle of the precession in relation to the steady state is small, the Landau-Lifshitz-equation (14) is linear, thus it is referred to as linear Ferromagnetic Resonance. For large deflection angles this phenomenon becomes nonlinear (see [5]), but it will not be discussed in this paper.

FMR spectroscopy is an important technique to analyze spin wave resonance and magnetization dynamics in different magnetic materials.

2.2 Spin Waves

The phenomenon of spin waves arises when the precession of one magnetic moment in a magnetic material is transferred to adjacent magnetic moments, causing them to precess as well, and this process continues until all magnetic moments in the material are excited. A visual representation of this propagating spin wave is shown in Fig. (4).

Spin waves is the collective oscillation of the magnetic moments and the direct consequence of the low-energy excitations of the exchange-coupled spins. Interestingly, in certain materials, the orbital angular momentum is fully compensated and only the uncompensated spins contribute to these oscillations [5, p. 23]. When the precessions of the magnetic moments are not in phase, the phenomenon is referred to as 'spin wave' and its quantized quasiparticle is called 'magnon'. The whole field of Magnonics is named after this

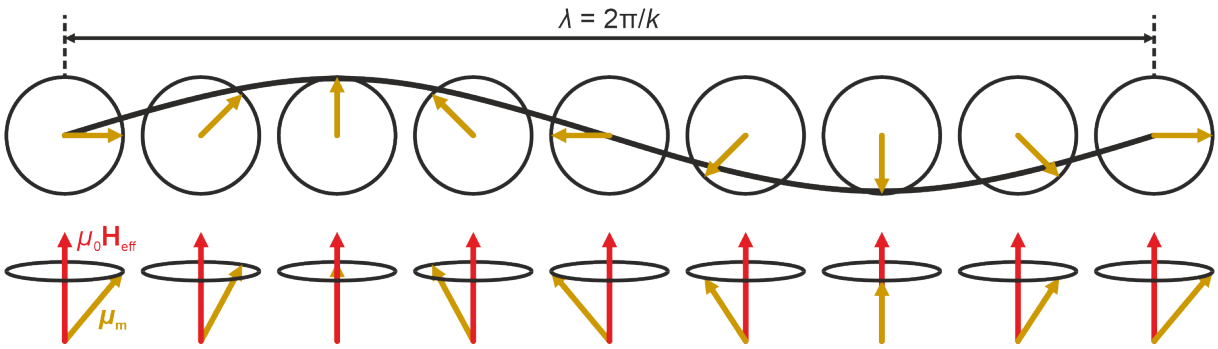

Figure 4: Illustration of a propagating spin wave as viewed from above and from the side. The magnetic moments $\boldsymbol{\mu}_\mathrm{m}$, shown as yellow arrows, precess around the steady state or the direction of the external magnetic field $\boldsymbol{H}_\mathrm{eff}$ (red arrows) and the phase of neighboring spins varies along the direction of propagation. Also the definition of the wavelength λ of the spin wave is shown. Reprinted from [9].

quasiparticle. Magnons behave as bosons (i.e., with spin $\boldsymbol{S} = 1$) and thus have mass [4], [7].

Spin waves can be described by their wavelength λ, amplitude and phase and most importantly, the wave vector k, which points in the direction of the wave propagation. In low-loss ferromagnetic films, the distance over which the wave propagates can be much greater than its wavelength [10]. Due to wave-particle duality, the following formulas can be correlated.

The quasi-momentum:

$$\boldsymbol{p} = \hbar \boldsymbol{k} \tag{23}$$

The magnitude of the wave vector $\boldsymbol{k}$, expressed with the wavelength λ of the spin wave:

$$k = |\boldsymbol{k}| = \frac{2\pi}{\lambda} \tag{24}$$

The energy ϵ of a magnon with the reduced Planck constant $\hbar$ and the angular frequency ω, can be further expressed with the wave vector k and the exchange constant η [7, p. 200]:

$$\epsilon = \hbar\omega = \frac{p^2}{2m} = \hbar\eta k^2 = \frac{\eta p^2}{\hbar} \tag{25}$$

From this it follows, that the mass of a magnon is $m_\mathrm{mag} = \hbar/2\eta$ [7, p. 200], so about 5 times the mass of an electron.

2.3 Dispersion Relation

Two energies are identified as significant contributors to the formation of spin waves, the exchange energy, originating on the alignment of adjacent spins, and the dipolar energy, related to the dipole-dipole interaction. The dispersion spectrum of spin waves is governed by these interactions. Depending on the wavelength of a spin wave, one of the energies contributes more than the other. For short wavelengths, the exchange energy dominates due to its short range and for long wavelengths, the weaker dipolar energy with its further reach is predominant. So depending on the wavelength of the spin waves, only one of those interactions has to be considered and respectively, the spin waves are called exchange or dipolar spin waves. Spin waves typically have wavelengths in the range of mm to nm [1]. The dispersion relation of spin waves $\omega = \omega(k)$ describes the dependency of frequency ω on the magnitude of the wave vector $k = |\boldsymbol{k}|$.

We can gain the phase velocity v_p (eq.(26)) from the ratio of ω and k and the group velocity v_g (eq.(27)) from the derivation of the dispersion relation [5, p. 120]. The phase velocity represents the speed at which a single phase of the wave propagates through space, while the group velocity describes the speed of the envelope of the wave packet of spin waves and in lossless media, it also corresponds to the energy propagation velocity [5, p. 124].

$$v_\mathrm{p} = \frac{\omega}{k} \tag{26}$$

$$v_\mathrm{g} = \frac{d\omega}{dk} \tag{27}$$

For comparison, the dispersion relation of electromagnetic waves, such as light in a vacuum, with velocity equal to the speed of light $v_\mathrm{light} = c$ is linear, so the frequency ω_light is directly proportional to the wave vector k_light, as described by the relation $\omega_\mathrm{light} = ck_\mathrm{light}$. In this case, the phase velocity $v_\mathrm{p,light}$ and the group velocity $v_\mathrm{g,light}$ are identical, as shown in equation (28)) [11, p. 77].

$$v_\mathrm{p,light} = \frac{\omega_\mathrm{light}}{k_\mathrm{light}} = v_\mathrm{g,light} = \frac{d\omega_\mathrm{light}}{dk_\mathrm{light}} = c \tag{28}$$

In contrast to electromagnetic waves, spin waves exhibit a nonlinear dispersion relation, due to the interplay of exchange interactions, dipolar interactions, and external magnetic fields. Also, spin wave dispersions are characterized by a non-zero frequency at zero wave

vector $k = 0$ corresponding to FMR. This FMR frequency represents the minimum energy threshold required for spin wave excitation. As a result, spin wave modes below the FMR frequency are not supported, as a minimum energy is needed to overcome the internal magnetic field within the magnetic material [5].

Furthermore, the dispersion relation also depends on the alignment of a magnetic material in an external magnetic field, here we consider a thin magnetic film. Specifically, it is determined by the orientation of the wave vector $\boldsymbol{k}$, which describes the direction of the spin wave propagation, relative to the direction of the applied external magnetic field $\boldsymbol{B}_{\text{ext}}$. The dispersion relation is also influenced by the saturation magnetization M_{S}, the exchange constant A_{ex}, the boundary or pinning conditions, and sample thickness d.

We can discern different modes of spin wave alignments relative to the direction of the applied magnetic field: Damon-Eshbach Magnetostatic Spin Waves, Forward Volume Magnetostatic Spin Waves and Backward Volume Magnetostatic Spin Waves (see Fig.5).

Damon-Eshbach Magnetostatic Spin Waves (DE), also referred to as Magnetostatic Surface Spin Waves, are excited when a thin magnetic film is magnetized in-plane and the spin waves propagate perpendicular to the magnetic field $\boldsymbol{B}_{\text{ext}}$. So, the wave vector k, representing the direction of spin wave propagation, is perpendicular to the direction of the magnetic field $\boldsymbol{B}_{\text{ext}}$ and thus the saturation magnetization M_{S}. The group velocity v_{g} and the phase velocity v_{p} of the spin waves travel in the same direction, which are therefore referred to as forward waves. One defining characteristic of these spin waves is the fact, that their amplitude has a maximum at the surface of the film which drops off exponentially towards the middle of the film. This is why this mode is referred to as surface spin waves [5, p. 162].

The following two modes, in contrast to the surface spin waves of DE, expand through the volume of the film, that is why they are called "Volume".

Forward Volume Magnetostatic Spin Waves (FV) are created in the case that the film is magnetized out-of-plane and the spin waves propagate perpendicular to the magnetic field $\boldsymbol{B}_{\text{ext}}$ and the saturation magnetization M_{S}. The group velocity v_{g} and the phase velocity v_{p} are aligned in the same direction, so these spin waves are also forward waves [5, p. 151]. The waves are propagating throughout the volume of the film sinusoidally.

Backward Volume Magnetostatic Spin Waves (BV) occur in the case the film is

magnetized in-plane and propagate parallel to the external magnetic field $\boldsymbol{B}_{\text{ext}}$. An important characteristic is that the group velocity v_{g} and the phase velocity v_{p} are antiparallel to each other, referred to as backward wave. The phase velocity is aligned with the wave vector k, while the group velocity is aligned antiparallel to k. This is seen in the dispersion relation as a negative slope of the curve (see Fig.5) [5, p. 158]. In this configuration, again the waves are propagating throughout the volume of the film sinusoidally.

As a side note, a very good visualization of a wave where the group velocity and the phase velocity travel in opposite directions is found on the Wikipedia website on group velocity [12].

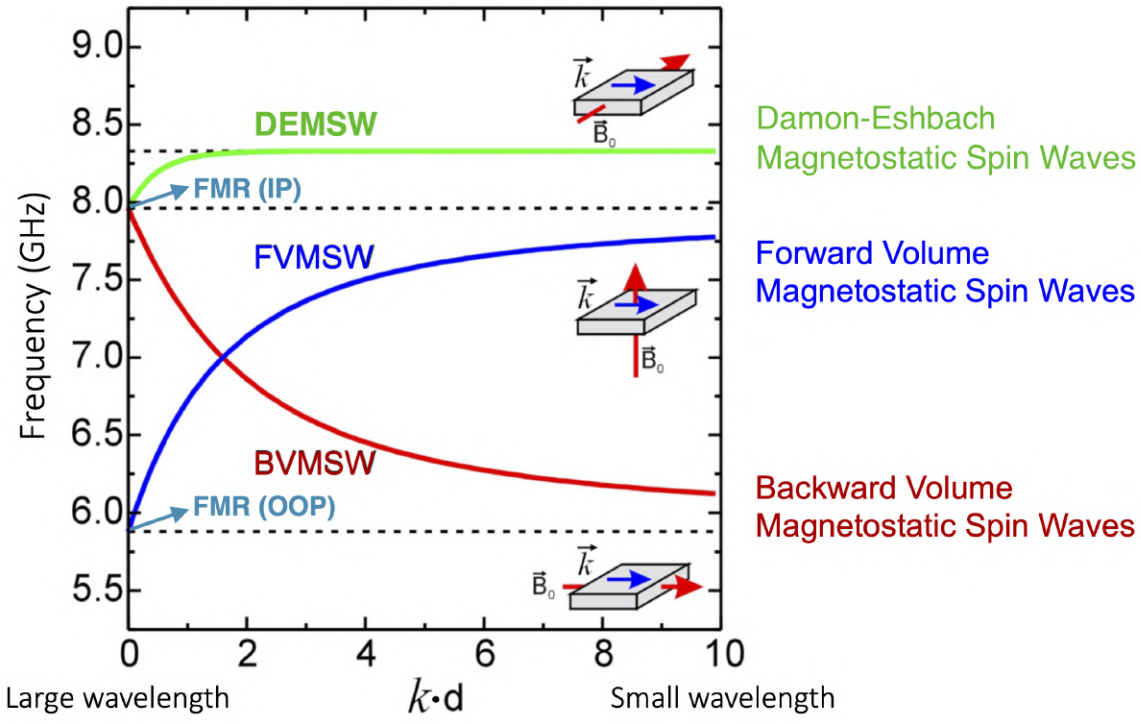

Figure 5: The graph shows the dispersion relations of dipolar spin waves for the different geometries: DE, FV, BV modes and their corresponding configurations. The dispersion relation is represented by the spin wave frequency as a function of wave number k multiplied by the thickness of the thin film d. FMR for in-plane (IP) and out-of-plane (OOP) magnetization is indicated exactly on the y-axis since k=0 in this case. Reprinted and adapted from [13, p. 13].

2.4 Perpendicular Standing Spin Waves

Another important mode of FMR for higher-order modes occurs when the wave vector has a component perpendicular to the surface of the magnetic film. The confinement along the thickness of the film leads to the formation of quantized standing spin waves, a phenomenon also known as **Perpendicular Standing Spin Waves** (PSSW) [14].
These spin waves are non-propagating, with a wave vector component equal to zero in the film plane. They are reflected at the confining surfaces of the film, resulting in constructive interference and the formation of standing spin waves. Due to the finite thickness of the film, only specific modes fulfill the boundary conditions, leading to a quantized mode spectrum [7, p. 189].
The quantization of the spin waves can be described by the wave number k_n in eq.(29) with the quantization number n along the thickness of the film d and the wave number k_m with quantization number m for the width w as shown in Fig.7.

$$k_\mathrm{n} = \frac{n\pi}{d} \tag{29}$$

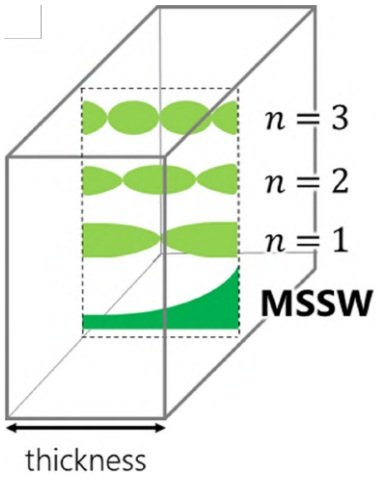

Figure 6: Illustration of the PSSW modes (n = 1,2,3) in light green and the Magnetostatic Surface Spin Waves (MSSW) or DE mode amplitudes in dark green for a thin ferromagnetic film with the relevant thickness. Reprinted from [15].

The boundary conditions, also referred to as spin pinning conditions, define whether the magnetic moments can precess at the film surface (unpinned modes) or cannot precess at the film surface and remain fixed (pinned modes). More precisely, for unpinned modes, the number of standing spin wave nodes across the film thickness is given by $n = 0, 1, 2, \ldots,$

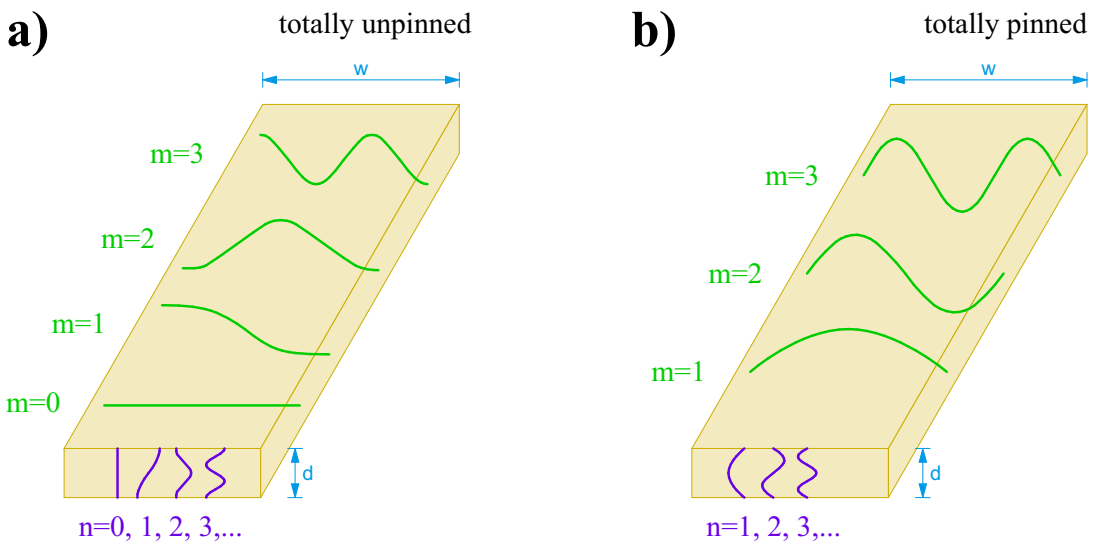

Figure 7: Quantization of spin waves at the surface boundaries in a waveguide with thickness d and width w, illustrated for the cases of a) totally unpinned and b) totally pinned spin wave modes. Based on [7, p. 191, Fig.7.6].

where the node $n = 0$ corresponds to FMR described in Chapter 2.1. In contrast, for pinned boundary conditions, the allowed modes are restricted to the nodes $n \in \mathbb{N}$, which excludes the FMR mode [7, p. 190]. PSSW are defined for $n \neq 0$, and thus describe standing modes confined across the film thickness. As such, they do not represent propagating spin waves and cannot be described by the same dispersion relations.

In experiments, purely pinned or unpinned modes rarely occur. Instead, partially pinned modes are observed due to surface anisotropy at the film interfaces. However, in most cases, it is sufficient to assume totally unpinned modes for an accurate calculation. The angular frequency of the PSSW can be expressed by eq.(30) [7, p. 193], [16] with eq.(21) and eq.(22) and the exchange stiffness λ_{ex}:

$$\omega_{\mathrm{PSSW}} = \sqrt{\left(\omega_{\mathrm{H}} + \omega_{\mathrm{M}}\lambda_{\mathrm{ex}}\left(\frac{n\pi}{d}\right)^2\right)\left(\omega_{\mathrm{H}} + \omega_{\mathrm{M}}\lambda_{\mathrm{ex}}\left(\frac{n\pi}{d}\right)^2 + \omega_{\mathrm{M}} sin^2\Theta\right)} \tag{30}$$

where A_{ex} denotes the Heisenberg exchange constant, the wave number k_{n} is expressed by eq.(29), and the exchange stiffness λ_{ex} is calculated as:

$$\lambda_{\mathrm{ex}} = \frac{2A_{\mathrm{ex}}}{\mu_0 M_{\mathrm{S}}^2} \tag{31}$$

In the equation eq.(30), the angle Θ distinguishes between different magnetization con-

figurations. For a film magnetized IP relative to the direction of the external magnetic field, the angle is $\Theta = \pi/2$, whereas for the OOP case, the angle is $\Theta = 0$. The angular frequency ω can be expressed in terms of the linear frequency $f = \omega/2\pi$, leading to distinct formulations for the IP and OOP configurations (eq.(32) and eq.(33)). The IP case (eq.(32)) is also referred to as Herring-Kittel formula.

$$f_{\mathrm{PSSW,IP}} = \frac{\gamma}{2\pi}\sqrt{\left(B_{\mathrm{ext}} + \frac{2A_{\mathrm{ex}}}{M_{\mathrm{S}}}\left(\frac{n\pi}{d}\right)^2\right)\left(B_{\mathrm{ext}} + \frac{2A_{\mathrm{ex}}}{M_{\mathrm{S}}}\left(\frac{n\pi}{d}\right)^2 + \mu_0 M_{\mathrm{S}}\right)} \tag{32}$$

$$f_{\mathrm{PSSW,OOP}} = \frac{\gamma}{2\pi}\sqrt{\left(B_{\mathrm{ext}} + \frac{2A_{\mathrm{ex}}}{M_{\mathrm{S}}}\left(\frac{n\pi}{d}\right)^2 - \mu_0 M_{\mathrm{S}}\right)} \tag{33}$$

Note that even in propagating-spin-wave experiments on magnetized thin film samples, the finite film thickness enforces PSSW quantization. Since in the FV geometry, the bias field and of the spin wave propagation direction both are oriented OOP and thus along the film thickness, the PSSW modes are more enhanced in comparison to IP (DE or BV) configurations. Higher-order PSSW modes (n$\geq$ 2) are often too weakly excited to appear as distinct peaks in propagating spin wave measurements [17].

The next chapter explains the appropriate dispersion relation describing the propagating spin waves.

2.5 Kalinikos-Slavin Model

Before the Kalinikos-Slavin model (K.S. model) was developed in 1986, the dispersion relation of spin waves was usually calculated by solving the LL-eq. using the eigenfunction method. This calculation had to be conducted separately for the idealized boundary conditions of either totally pinned or totally unpinned surface spin waves, which was either inconvenient or overly restrictive (according to [10]).

The K.S. model [10] was introduced as an analytical method which is able to determine the dipole-exchange spin wave propagation. The model can describe both, exchange-dominated spin waves, which favor short wavelengths, and dipolar spin waves, which are biased toward long wavelengths, in thin films with either totally pinned or totally unpinned boundary conditions.

Additionally, the K.S. model is useful for calculating IP spin wave propagation at arbitrary angles. Additionally, it can also be applied to higher spin wave modes that propagate in

one direction along the magnetic film but are also quantized due to the film's thickness in the perpendicular direction. Therefore, the wave number must account for both the tangential component k_t, which represents the propagation direction, and the perpendicular component k_n which depends on the film's thickness d. This leads to the total wave number given by $k^2 = k_\mathrm{t}^2 + k_\mathrm{n}^2$.

The following comprehensible summary of the paper of Kalinikos-Slavin [10] is based, with permission, on [18].

The dispersion relation according to the K.S. model [10] is given by:

$$\omega = \sqrt{(\omega_\mathrm{H} + \omega_\mathrm{M}\lambda_\mathrm{ex}k^2)(\omega_\mathrm{H} + \omega_\mathrm{M}\lambda_\mathrm{ex}k^2 + \omega_\mathrm{M}F_\mathrm{n})} \tag{34}$$

where the expression F_n is

$$F_\mathrm{n} = sin^2\Theta + P_\mathrm{n}\left(cos2\Theta + sin^2\Theta sin^2\varphi\left(1 + \frac{\omega_\mathrm{M}(1-P_\mathrm{n})}{\omega_\mathrm{H} + \omega_\mathrm{M}\lambda_\mathrm{ex}k^2}\right)\right) \tag{35}$$

Here, Θ is the azimuthal angle which determines the magnetization orientation of the thin film relative to the external magnetic field (with in-plane $\Theta = 0$ and out-of-plane $\Theta = \frac{\pi}{2}$). In the IP case, the angle between the direction of propagation and the effective magnetic field is given by the polar angle φ.

For the important configurations of propagating spin waves, described in Chapter 2.3, the angles are: DE: $\Theta = \frac{\pi}{2}$ and $\varphi = \frac{\pi}{2}$, BV: $\Theta = \frac{\pi}{2}$ and $\varphi = 0$, and FV: $\Theta = 0$.

The dispersion relation in eq.(34) can be expressed as a linear frequency by using eq.(21) and eq.(22) and replacing the exchange stiffness λ_ex by applying eq.(31). This yields the following:

$$f = \frac{\gamma}{2\pi}\sqrt{\left[B + \frac{2A_\mathrm{ex}}{M_\mathrm{S}}\left(k_\mathrm{t}^2 + \left(\frac{n\pi}{d}\right)^2\right)\right]\left[B + \frac{2A_\mathrm{ex}}{M_\mathrm{S}}\left(k_\mathrm{t}^2 + \left(\frac{n\pi}{d}\right)^2\right) + \mu_0 M_\mathrm{S}F_\mathrm{n}\right]} \tag{36}$$

with the new expression for F_n:

$$F_\mathrm{n} = sin^2\Theta + P_\mathrm{n}\left(cos2\Theta + sin^2\Theta sin^2\varphi\left(1 + \frac{\mu_0 M_\mathrm{S}(1-P_\mathrm{n})}{B + \frac{2A_\mathrm{ex}}{M_\mathrm{S}}\left(k_\mathrm{t}^2 + (\frac{n\pi}{d})^2\right)}\right)\right) \tag{37}$$

The function P_n is crucial because it incorporates the spin-pinning conditions.

So for the case of totally unpinned surface spins, where $n = 0, 1, 2, \ldots$, the function P_n is:

$$P_{\mathrm{n}} = \frac{k_{\mathrm{t}}^2}{k_{\mathrm{t}}^2 + (\frac{n\pi}{d})^2} \left(1 - \frac{2k_{\mathrm{t}}(1-(-1)^n e^{-k_{\mathrm{t}}d})}{d(k_{\mathrm{t}}^2 + (\frac{n\pi}{d})^2)} \frac{1}{1+\delta_{0\mathrm{n}}} \right) \tag{38}$$

where $\delta_{0\mathrm{n}}$ is the Kronecker-Delta. In the special mode of FMR, it is referred to as 'zero mode' due to the indices of the Kronecker-Delta and resulting in $\delta_{00} = 1$.

For the case of totally pinned spins ($n = 1, 2, 3, \dots$) the function P_{n} becomes:

$$P_{\mathrm{n}} = \frac{k_{\mathrm{t}}^2}{k_{\mathrm{t}}^2 + (\frac{n\pi}{d})^2} \left(1 + \frac{2(\frac{n\pi}{d})^2(1-(-1)^n e^{-k_{\mathrm{t}}d})}{k_{\mathrm{t}}d(k_{\mathrm{t}}^2 + (\frac{n\pi}{d})^2)} \right) \tag{39}$$

The dispersion relation of spin wave modes is useful for determining various important quantities of the spin waves, such as the group velocity v_{g}, lifetime, and decay length.

3 Yttrium-Iron-Garnet

This chapter is a brief description of the magnetic materials, with a particular focus on the ferrimagnetic material of Yttrium-Iron-Garnet (YIG), which is a widely used material in the field of magnonics because of its advantageous properties. The main sources for this chapter are [4], and [3].

Magnetic materials are categorized by their type of magnetic order, with ferromagnets, antiferromagnets, and ferrimagnets representing distinct classes, each primarily characterized by a specific alignment of atomic magnetic moments. These magnetic materials are a huge group of interest used in spin wave research.

Ferromagnets can be defined by inherent parallel magnetic moments with the same magnitude (explained by the molecular fields of the Weiss theory [4, p. 102]) and spontaneous net magnetization. In antiferromagnets and ferrimagnets, magnetic moments are aligned antiparallel in their two sub-lattices. Ferrimagnets are characterized by having two sublattices with different net magnetization, resulting in the display of a spontaneous net magnetization. In contrast, antiferromagnets have two equally but oppositely magnetized sublattices, leading to complete compensation and a net magnetization of zero.

Ferrites and magnetic garnets are important for microwave device applications. Ferrites are usually ferrimagnetic ceramic compounds derived from iron oxides and show a high electrical resistivity. A widely used ferrite and among the oldest known magnetic materials (used as compass needle in China around 3500 years ago) is magnetite (Fe_3O_4) [4, p. 124, p. 132].

In this paper, we focus mainly on YIG, the 'miracle material' [3], with the chemical composition $Y_3Fe_5O_{12}$ [4, p. 146]. YIG is an iron-based ferrimagnetic insulator, with a cubic crystalline structure composed of two sublattices. The magnetic properties arise solely from the uncompensated Fe_5^{3+} ions, which are distributed on two sub-lattices and aligned antiparallel. Three iron ions are on one sub-lattice and two are positioned antiparallel on the other sub-lattice which results in spontaneous magnetization. This results in a relatively low saturation magnetization of approximately 140 kA/m [1, p. 7]. In the ground state, the iron ions have no net orbital angular momentum; therefore, the spin angular momenta and consequently the gyromagnetic ratio $\gamma/2\pi = \gamma_S/2\pi = 28$ GHz/T are the sole contributors to the magnetic moments in YIG [5, p. 23].

YIG is typically grown on a Gallium-Gadolinium-Garnet (GGG) substrate to ensure lat-

tice matching and high crystal quality [5, p. 19]. GGG is also almost transparent which is useful in certain experiments [1].

One of the most notable properties of YIG is its exceptionally low Gilbert damping parameter of $\alpha \sim 10^{-4}$, enabling longer spin wave lifetimes compared to other materials. This low damping also leads to a very narrow FMR linewidth, making YIG highly suitable for magnonic applications.

An additional advantage of the material is its high Curie temperature ($T_C \sim 560$ K), which ensures thermal stability up to degrees far above room temperature [1].

In the experiments presented in this work, the FMR measurements (see Chapter 5) were conducted using a microstrip antenna, while the PSWS measurements (see Chapter 6) employed a pair of inductive transducers placed on nanometer-thin YIG films to excite and detect spin wave propagation.

4 Vector Network Analyzer and S-Parameters

This chapter provides an overview of the principles of a Vector Network Analyzer (VNA) and its application in the quantitative measurement and analysis of spin wave signals. The VNA is an essential instrument for radio-frequency and high-frequency applications, playing a key role in modern wireless technology. They are used to validate simulations, as well as testing prototypes of components or devices [19].

Additionally, the fundamentals of the scattering parameters, which are the key measured quantities in VNA experiments, are explained with focus on transmission and reflection parameters, based on [20]. These parameters are essential for characterizing the propagation and attenuation of spin waves in the investigated structures.

4.1 Vector Network Analyzer

In the experiments conducted for this thesis, a VNA is used to analyze spin waves in magnetic samples. The manufactured samples, including the integrated microwave antennas, are often referred to as the device under test (DUT). This term is commonly used for radio frequency or higher-frequency components that are examined for specific characteristics [19]. The VNA generates microwave frequencies, typically extending into the tens of GHz, necessary to excite spin waves and subsequently detects the resulting signals. In FMR, for example, the VNA enables analysis by detecting the resonant absorption of microwaves by the magnetic system of the examined sample.

The VNA used in this experiment is equipped with two ports, which are connected via coaxial cables to an antenna, either a stripline or transducers, depending on the specific experimental setup to conduct the measurements. The DUT is placed in a static, homogeneous magnetic field $\boldsymbol{B}_{\text{ext}}$, which aligns the saturation magnetization within the sample. Each port (port 1 and port 2) of the VNA sends microwave signals, in the form of alternating electrical currents, to the antenna connected directly to the magnetic sample. This generates a small, locally applied dynamic magnetic field $\boldsymbol{b}_{\text{ext}}(t)$. Spin waves are excited when the frequency of the input microwave signal matches the corresponding dispersion relation. The input signals are then either reflected back to the same port, transmitted to the other port, or absorbed by the magnetic material. This process allows for the determination of the output power, which corresponds to the transmitted spin waves, by

comparing it with the input power in the form of microwaves. The VNA measures the amplitudes and phases of the signals generated and detected at both ports, enabling the calculation of phase differences and phase shifts. By evaluating the differences between the input and output powers, we can assess the efficiency of spin wave transmission and gain insights into the interaction between the microwaves and the magnetic system of the sample.

High frequency coaxial cables are used especially to counter the skin effect, which is the distribution of an alternating electric current mainly near the surface of a conductor cable instead of evenly spread across the cross section of the whole cable. An important quantity to consider is the characteristic impedance of conductors. The impedance that minimizes signal loss for a high-frequency coaxial cable results in an overall impedance of 50 Ω of the system including the DUT.

The wave number (and thus the spin wave dispersion relation) can be determined based on the dimensions of the antennas. The size of the antennas dictates the wavelengths or frequencies of the waves they can effectively excite or detect. Since the antenna dimensions are typically designed to match the wavelength of the spin waves, the dimensions directly influence the wave number, which in turn defines the spin wave properties and dispersion relation, as described by the K.S. model described in Chapter 2.5.

4.2 Scattering Parameters

It is more convenient for high frequencies to regard the input and output signals as waves instead of voltages and currents. Similar to how an incident light wave is either reflected or transmitted through glass, the incident electromagnetic wave from a VNA port is being reflected or transmitted upon encountering the DUT with its characteristic load impedance Z_{L} (load impedance). If there is a mismatch between the DUT impedance and the network's characteristic impedance Z_{G} (generator impedance), which is typically 50 Ω), the microwave signals are 'scattered'.

The measurements conducted by the VNA are gathered as so-called scattering parameters or S-parameters and are represented by the complex scattering matrix S (see eq.(40)). So the components of the vectors $(\vec{a})$ and $(\vec{b})$ correspond to the input and output signals in the ports 1 and 2, respectively. A conceptual illustration is shown in Fig.8.

$$\begin{pmatrix} b_1 \\ \\ b_2 \end{pmatrix} = \begin{pmatrix} S_{11} & S_{12} \\ \\ S_{21} & S_{22} \end{pmatrix} \begin{pmatrix} a_1 \\ \\ a_2 \end{pmatrix} \tag{40}$$

The components of the scattering matrix S are defined as the ratios of the output signals to the input signals, corresponding to the specific transmitting and receiving ports.
The S-parameters S_{11} and S_{22} describe the reflection at the same port, i.e., reflection from port 1 to port 1 and from port 2 to port 2. These are calculated as follows:

$$S_{11} = \left.\frac{b_1}{a_1}\right|_{a_2=0} \quad , \quad S_{22} = \left.\frac{b_2}{a_2}\right|_{a_1=0} \tag{41}$$

In the case of a DUT with impedance Z_L connected to a VNA of impedance $Z_\mathrm{G} = Z_0$, these reflection coefficients S_{11} and S_{22} are also denoted by the reflection factor Γ, which is defined as:

$$\Gamma = \frac{Z_\mathrm{L} - Z_0}{Z_\mathrm{L} + Z_0} \tag{42}$$

where Z_L is the load impedance (DUT impedance) and impedance Z_0 is the characteristic impedance of the network (50 Ω)).
And the transmission S-parameters S_{12} and S_{21} describe the transmission between different ports, i.e., from port 1 to port 2 and from port 2 to port 1. They are calculated as:

$$S_{12} = \left.\frac{b_1}{a_2}\right|_{a_1=0} \quad , \quad S_{21} = \left.\frac{b_2}{a_1}\right|_{a_2=0} \tag{43}$$

The transmission factor T (for S_{12} and S_{21}) is defined as:

$$T = \frac{2Z_0}{Z_0 + Z_\mathrm{L}} \tag{44}$$

In the ideal case of no losses, that means no energy dissipation in a system where the incident signal is either reflected, transmitted, or absorbed, we have the relation:

$$\Gamma + \mathrm{T} = 1 \tag{45}$$

To summarize, the reflection and transmission parameters describe the following:

- S_{11} and S_{22}: The reflection factor Γ represents the ratio of the reflected signal to the incident signal at the same port. It is caused by the impedance mismatch between the DUT and the VNA. $\Gamma = 0$: no reflection of the signal (impedance match), $\Gamma = 1$: the signal is completely reflected (impedance mismatch)

- S_{12} and S_{21}: The transmission factor T (S_{12} represents the fraction of the incident signal that is transmitted through the DUT to the other port: $T_{2\to1}$, S_{21}: $T_{1\to2}$), $T = 0$: no transmission of the signal, $T = 1$: the signal is completely transmitted

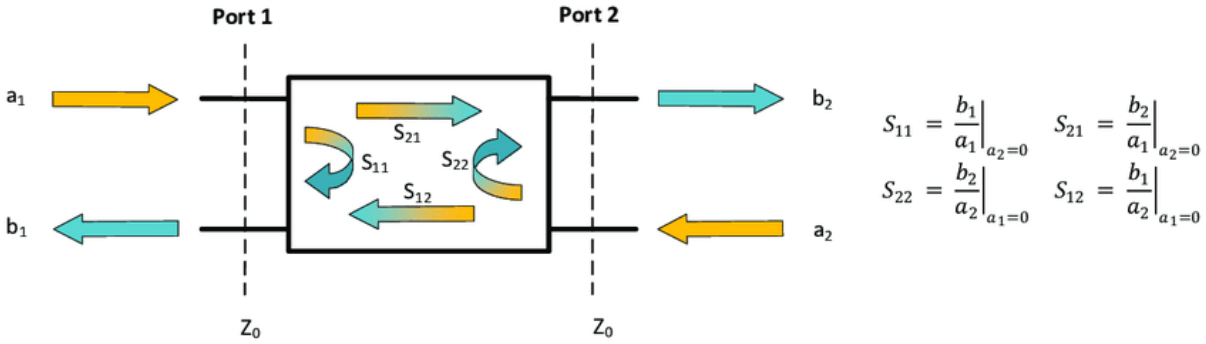

Figure 8: Schematic of reflected and transmitted signals of the two-port VNA inside a DUT, represented by the box. The input signals are represented by a_1 and a_2 and the output signals by b_1 and b_2. Z_0 is the required impedance of 50 Ω. The S-parameters are calculated with the shown formulas. Reprinted from [21].

The reflection S-parameters S_{11} and S_{22} can be used to assess the impedance match of a DUT correlated with the network reference impedance (50 Ω). For example, some devices are supposed to allow the transmission of signals only in one direction, while minimizing reflections from the load back to the generator (return loss).
Often, only the S-parameters S_{12} or S_{21} are considered in measurements, because they contain the information of the transmission of signals between the two ports, which is especially interesting for the detection of spin wave propagation.

5 Ferromagnetic Resonance - Measurements

A good starting point to attain foundations of the theoretical background and gaining experimental experience was the lab course, where the FMR of a thin YIG film was measured and analyzed using a VNA. Since this course coincided with the work on this bachelor thesis, the experiment and its findings are included in the following section.
The fundamental principles of FMR, including the role of the external and oscillating magnetic fields, are discussed in Chapter 2.1. Here, we focus on the experimental implementation and data analysis.
The primary objective of the FMR experiment, beyond reinforcing theoretical concepts, was to acquire measurement data of YIG. This data was then used to determine characteristic material parameters, including the Gilbert damping parameter, the inhomogeneous linewidth broadening, and the saturation magnetization.

5.1 Methodology

A sample of a thin YIG film is placed in-plane in an external static magnetic field $\boldsymbol{B}_{\text{ext}}$ to align all the magnetic moments in the direction of the field and achieve saturation magnetization. A smaller oscillating magnetic field $\boldsymbol{b}_{\text{ext}}(t)$ with a microwave frequency of around $\sim 10^9$ Hz is applied by using a VNA connected by two coaxial cables to a stripline antenna and to the sample, as shown in Fig.9. The oscillating magnetic field $\boldsymbol{b}_{\text{ext}}(t)$ is applied perpendicular to the external static magnetic field and induces a uniform precession of the magnetic moments, i.e., FMR.

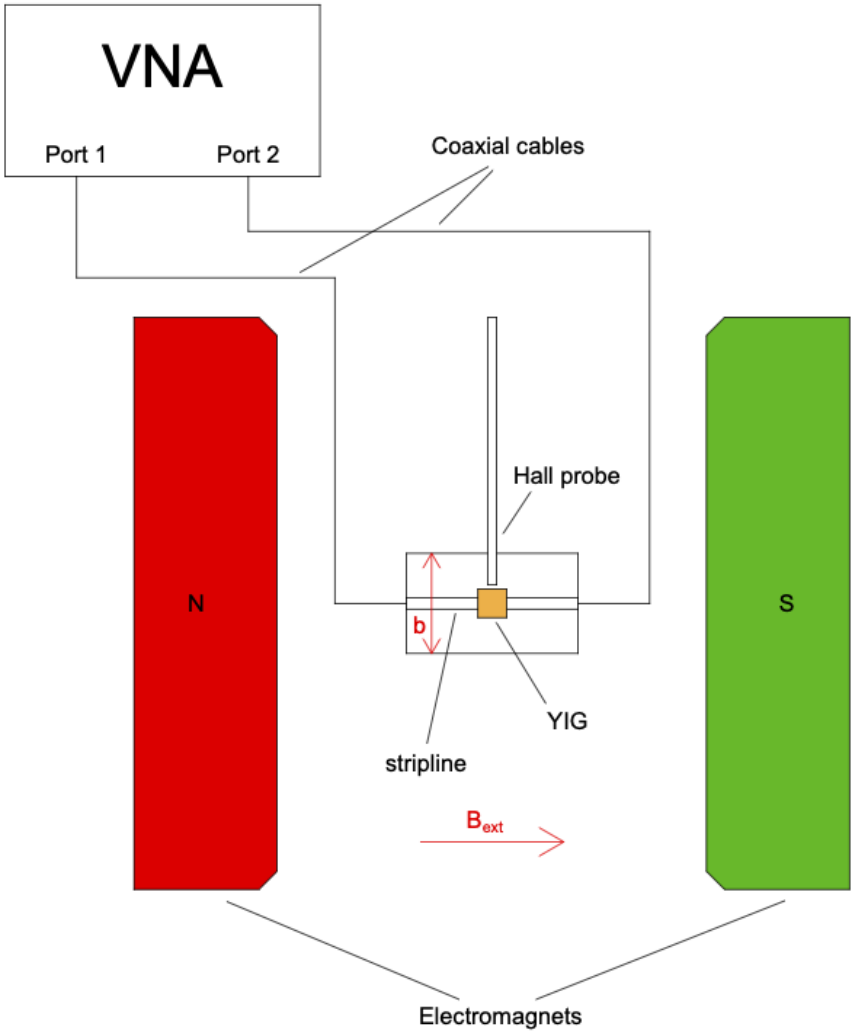

Figure 9: Sketch of the FMR setup showing the pole pieces of the electromagnet, two-port VNA, coaxial cables, Hall probe, stripline, YIG sample, and the directions of the applied external magnetic fields: the static magnetic field $\boldsymbol{B}_{\text{ext}}$ and the oscillating magnetic field $\boldsymbol{b}_{\text{ext}}(t)$.

5.2 Experimental Setup

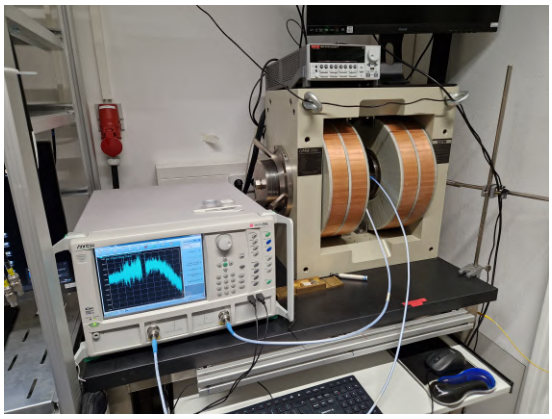

(a) Setup configuration with VNA, coaxial cables, and electromagnet

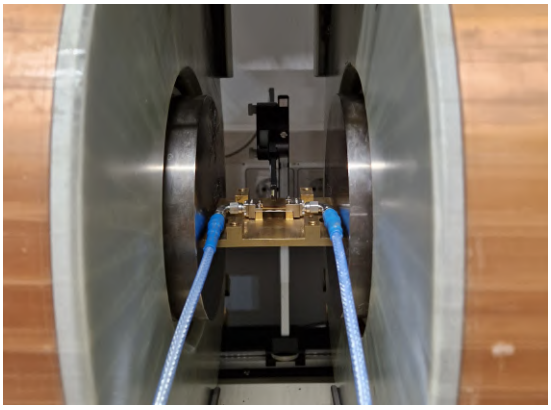

(b) Sample holder with connected coaxial cables between magnetic pole pieces

Figure 10: Photos of experimental setup

The lab at the university provides the following experimental setup to measure FMR: An H-frame electromagnet with two pole pieces manufactured by GMW Associates (Model 3473-70, 150 mm, 70 Amp Coils) is used to generate the external static magnetic field. The sample holder with the YIG film is placed in between the two pole pieces, so that it is positioned exactly in the middle and aligned IP with respect to the magnetic field. To monitor the magnetic field strength, a Hall probe (Gaussmeter) is placed close to the sample. The sample consists of the YIG film with 100 nm thickness with a stripline antenna positioned on top. The stripline antenna is used to transfer microwaves via a pair of coaxial cables connected to the VNA Vector Star by Anritsu (Model MS4642B) with a frequency range up to 20 GHz.

5.3 Measuring Process

First, the VNA was calibrated as instructed, using a calibration kit. Then the YIG sample was placed on the sample holder, and the starting frequency for a given external magnetic field was applied. The starting frequency was estimated beforehand by calculating and plotting the Kittel equation (18) for the IP magnetized thin film. Frequency sweeps were conducted using the VNA for 15 different values of the external magnetic field, ranging from from 20 mT to 600 mT. One important factor during the measurements was to gather enough data points per sweep by adjusting the frequency step size on the VNA,

so that at least $\sim$ 10000 points were reached to ensure a high resolution for the plot [22]. The VNA made a plot for each of the four S-parameters, but actually only the plot of the component S_{21} representing the transmission of the signal from Port 1 to Port 2 was relevant for the further evaluations.

Each frequency spectrum at a certain magnetic field B_{ext} showed a characteristic peak (actually dip, see Fig.11) in the S_{21} parameter plot, which corresponds to the Ferromagnetic Resonance of the YIG. The frequency range of the VNA was adjusted for each value of the magnetic field to get better and more exact FMR peaks. Also, to minimize the uncertainty, the background noise was immediately subtracted by the VNA from the transmission spectra. The plots and data points were saved for each of the different magnetic field for later assessment.

5.4 Results

5.4.1 FMR Peak with Lorentzian Fit

As an example, in Fig.11 the plot of the measured S_{21} S-parameter and the evaluated FMR peak for a magnetic field of 550 mT is shown. The curve was fitted with the Lorentzian function (eq.(46), this equation was given in the lab-course) using MATLAB.

$$S_{21} = y_0 + \frac{2A}{\pi} \frac{\Delta f}{4(f - f_{\text{FMR}})^2 + \Delta f^2} \tag{46}$$

S_{21} ... S-Parameter for transmission from port 1 to port 2 [dB]

y_0 ... constant

A ... constant

Δf ... linewidth in units of frequency [Hz]

f ... frequency [Hz]

f_{FMR} ... Ferromagnetic Resonance frequency [Hz]

The FMR peak for the applied magnetic field of $\boldsymbol{B}$ = 550 mT is located at $f_{\text{FMR}} = (18.04 \pm 0.01)$ GHz.

A Lorentzian fit was applied to each of the 15 measurements taken at different magnetic field values to determine the resonance frequencies (f_{FMR}) and linewidths (Δf), where

the linewidth corresponds to the full width at half maximum (FWHM) of the peak. The linewidths Δf were subsequently converted to units of magnetic field $\mu_0 \Delta H$ for further analysis.

The evaluated values of f_{FMR} and Δf are summarized in Table 1, which provides a detailed overview of the measurements and their corresponding fits. These results are used in the next chapter (see Chapter 5.4.2) to evaluate the damping parameter and inhomogeneous linewidth broadening.

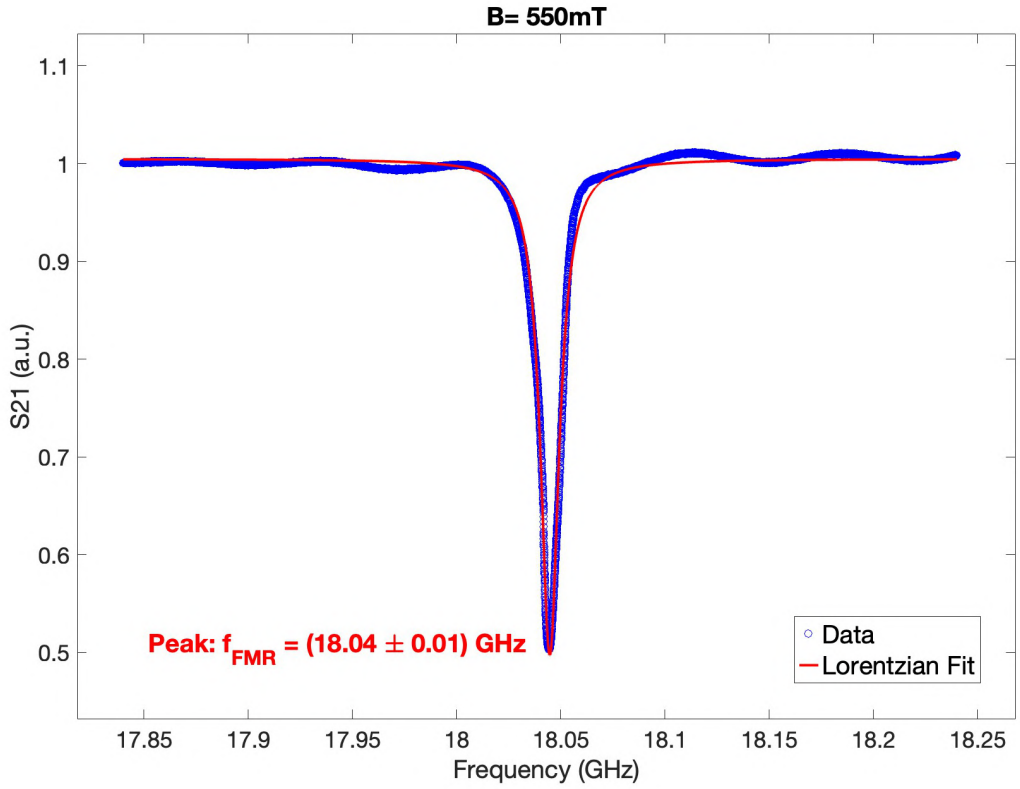

Figure 11: FMR of YIG detected at the magnetic field $\boldsymbol{B} = 550$ mT: the measured data (blue points) was fitted with the Lorentzian function (eq.(46)) (red line). The error bars for the measured data were too small. The maximum peak corresponds to the FMR-frequency f_{FMR} and in the case of the applied magnetic field $f_{\mathrm{FMR}} = (18.04 \pm 0.01)$ GHz.

#	$\boldsymbol{B}$ (mT)	f_{FMR} (GHz)	linewidth $\mu_0 \Delta H$ (mT)
1	20	1.84 ± 0.04	0.219 ± 0.005
2	25	2.09 ± 0.07	0.395 ± 0.008
3	50	3.11 ± 0.03	0.437 ± 0.005
4	75	4.00 ± 0.01	0.473 ± 0.002
5	100	4.83 ± 0.02	0.522 ± 0.003
6	150	6.40 ± 0.01	0.332 ± 0.001
7	200	7.91 ± 0.01	0.392 ± 0.002
8	250	9.39 ± 0.01	0.479 ± 0.002
9	300	10.85 ± 0.01	0.413 ± 0.001
10	350	12.30 ± 0.03	0.616 ± 0.006
11	400	13.75 ± 0.03	0.730 ± 0.005
12	450	15.18 ± 0.02	0.617 ± 0.003
13	500	16.61 ± 0.02	0.541 ± 0.003
14	550	18.04 ± 0.01	0.680 ± 0.002
15	600	19.47 ± 0.01	0.679 ± 0.002

Table 1: Table of the 15 measured values for the magnetic field **B** and the evaluated FMR frequencies f_{FMR} and linewidth $\mu_0 \Delta H$ in field units.

5.4.2 Extraction of Gilbert Damping Parameter and Inhomogeneous Linewidth Broadening

Next, all 15 different values of the linewidth $\mu_0 \Delta H$ were plotted against the corresponding FMR peak frequencies f_{FMR}. A linear fit was then applied using eq.(47) [23, p. 3] which was implemented in MATLAB.

$$\mu_0 \Delta H = \mu_0 \Delta H_0 + \frac{\alpha 4\pi f_{\mathrm{FMR}}}{\gamma} \tag{47}$$

μ_0 ... vacuum permeability, $\mu_0 = 1.257 \times 10^{-6} N/A^2$

ΔH ... linewidth in units of magnetic field [A/m]

ΔH_0 ... inhomogeneous linewidth broadening

α ... Gilbert damping parameter, unitless

f_{FMR} ... Ferromagnetic Resonance frequency [Hz]

γ ... gyromagnetic ratio, $\gamma = 28 \cdot 2\pi \cdot 10^9 rad/(s \cdot T)$

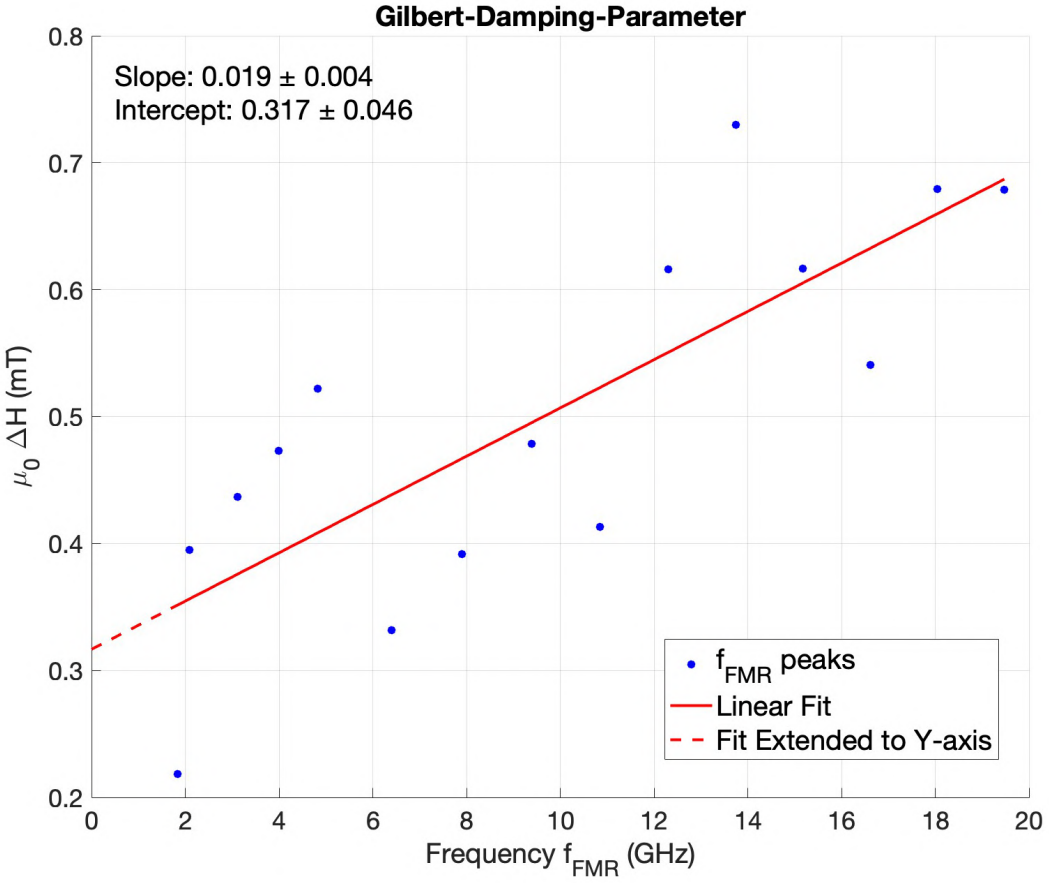

Figure 12: The damping parameter α and inhomogeneous linewidth broadening were evaluated by fitting a linear (red) line to the linewidth $\mu_0 \Delta H$ vs. FMR frequency (blue dots). The slope gives α, and the y-axis intercept corresponds to the inhomogeneous linewidth broadening. The scattering of the data points likely results from an inhomogeneous magnetic field. The error bars are too small to be displayed.

The Gilbert damping parameter $\alpha = 2.66 \times 10^{-4} \pm 0.56 \times 10^{-4}$ was calculated by taking the slope of the linear fit and applying eq.(47). Also, by extending the linear fit to the y-axis, the intercept gives the inhomogeneous linewidth broadening of ($\mu_0 \Delta H_0 = 0.317 \pm 0.046$) mT.

5.4.3 Saturation Magnetization of YIG

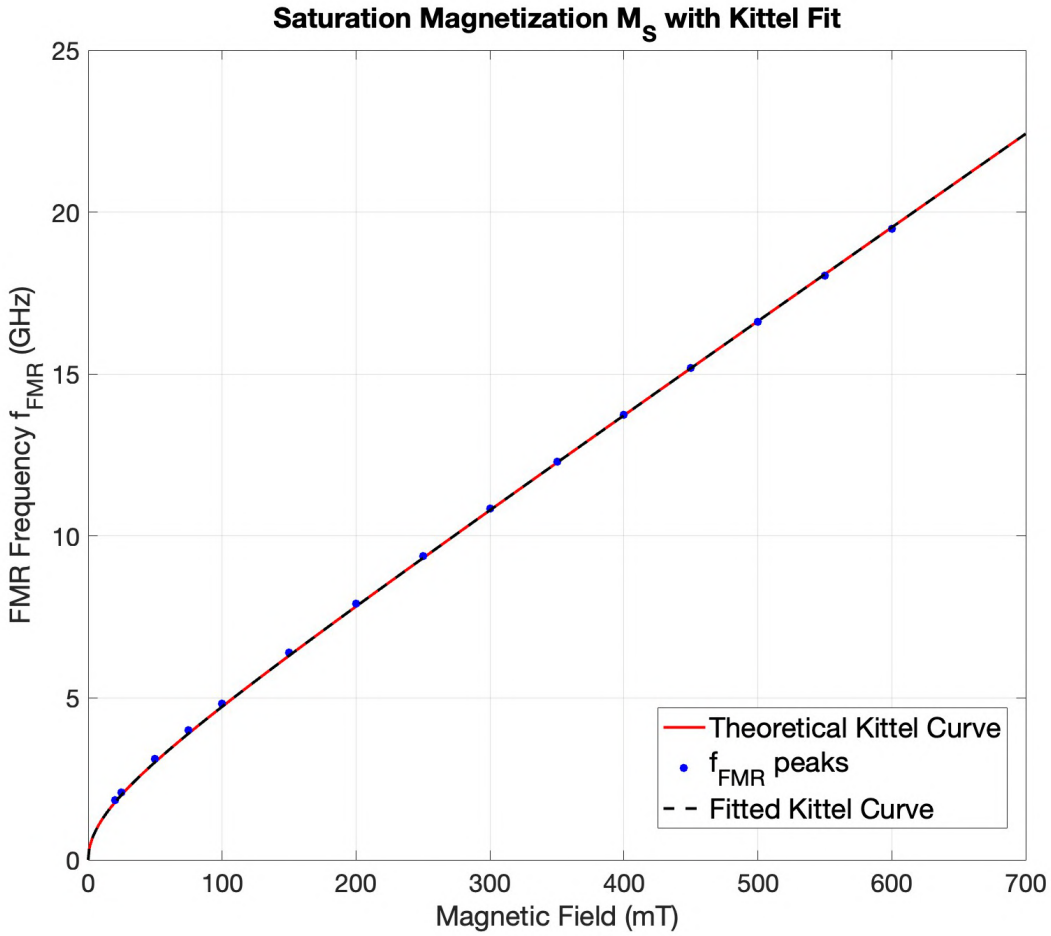

Figure 13: The saturation magnetization M_S was evaluated by fitting the FMR resonance frequencies f_{FMR} (blue dots) using the Kittel formula (black dashed curve) and compared to the theoretical Kittel formula (red curve). In order to achieve a better fit for the theoretical curve, the external magnetic field was adjusted by a 2.5% increase. The error bars are too small to be visible.

For the evaluation of the saturation magnetization M_S of the YIG sample, the FMR frequencies were plotted against the applied external field and fitted using the Kittel

equation (eq.(18)) in MATLAB. The theoretical Kittel curve (red curve shown in Fig.13) was plotted with the literature values for $\gamma/2\pi = 28$ GHz/T and $M_S = 140$ kA/m [1, p. 7]. A good agreement between the theoretical curve and experimental data was achieved by increasing the values of the external magnetic field B_{ext} by 2.5%, while keeping the literature values: $\gamma/2\pi = 28$ GHz/T and $M_S = 140$ kA/m.

5.5 Discussion

The evaluated Gilbert damping parameter is $\alpha = 1.484 \times 10^{-4}$, which is in good agreement with literature values for a 100 nm thin film of YIG, typically on the order of $\sim 10^{-4}$. Similarly, the inhomogeneous linewidth broadening expressed in units of the magnetic field, $\mu_0 \Delta H_0 = 0.317 \pm 0.046$ mT $= 3.17 \times 10^{-4} \pm 0.46 \times 10^{-4}$ T, also aligns well with literature values and falls within the expected range of approximately 10^{-4}T. The observed scattering of the data points is likely contributed to an inhomogeneous magnetic field across the sample.

Concerning the fit for the saturation magnetization, the values of the external magnetic field B_{ext} used in the fit were scaled by 2.5% increase compared to the measured values. This suggests that the magnetic field at the position of the sample was slightly lower than what was recorded by the Hall probe. A possible explanation for this deviation is the positioning of the sample exactly in the middle of the magnetic field, while the Hall probe was placed above the sample. Further support for this interpretation comes from the comparison with the theoretical Kittel curve, which also required a 2.5% increase in the applied field to achieve a good fit to the experimental data.

All the reference values for YIG were taken from [1, p. 7].

6 Propagating Spin Wave Spectroscopy - Measurements

This chapter focuses on the experiment of the measurement of **Propagating Spin Wave Spectroscopy** (PSWS), specifically investigating the DE, FV, and BV spin wave modes in a thin YIG film. The key objective of this thesis, however, was the design and construction of a novel sample holder enabling OOP measurements at the laboratory at the University of Vienna. This sample holder was tested for the IP and OOP configurations during the experiments and is described in detail in the following sections.

The PSWS experiment was conducted using microwave techniques with a VNA, which is a crucial tool for measuring spin wave transmission spectrum as a function of the input microwave frequency, which is why this technique is referred to as Propagating Spin Wave Spectroscopy.

The acquired PSWS data was correlated to the spin wave dispersion relation and the antenna excitation efficiency. This method was based on [24].

6.1 Methodology

For the PSWS experiment, a sample of a thin film of YIG is placed in an external static magnetic field B_{ext} and an oscillating magnetic field $b_{\text{ext}}(t)$ is applied. The magnetic field $b_{\text{ext}}(t)$ is created by a microwave frequency ($\sim 10^9$ Hz) sent by the VNA to the antenna. This causes excitation of spin waves in the YIG sample, which are captured as S-parameters by the VNA. The relevant S-parameter in this experiment was determined as S_{12} which is the transmission coefficient that describes the transmission of the input signals from port 2 through the DUT to port 1. This parameter was chosen because the measured transmitted signal exhibited a larger magnitude compared to the S_{21} signal for the DE mode.

After subtraction of the measured reference signal $S_{12,\text{ref}}$, S_{12} is usually converted to the dB scale for better visualization of the transmitted signal by using eq.(48) [24]. The reference signal is measured at $B_{\text{ext}} = 0$ T and a significant contribution to the background noise primarily comes from electromagnetic leakage caused by the coupling between the two antennas. Another contribution to the noise comes from different disturbances, e.g. from the coaxial cables or from the distance between the pole pieces of the electromagnet.

$$\Delta S_{12}(dB) = 20log_{10}(|S_{12} - S_{12,\text{ref}}|) \tag{48}$$

For each of the three measured modes (DE, BV, FV) the ΔS_{12} is further correlated with the associated dispersion relation and the excitation efficiency J_{exc} of the antenna.

The dispersion relation is calculated by applying the K.S. model (eq.(34)) with the following given values: YIG film thickness $d = 97$ nm, the exchange constant $A_{\text{ex}} = 3.6$ pJ/m, the gyromagnetic ratio $\gamma/2\pi = 28$ GHz/T, saturation magnetization: $M_{\text{S}} = 140$ kA/m, fundamental mode $n = 0$ and assuming fully unpinned spins at the surface as pinning condition.

The transducer excitation efficiency J_{exc} is calculated as the Fourier transform (eq.(49)) [24] of the normalized current density in an infinitely thin coplanar waveguide (CPW) transducer.

$$J_{\text{exc}} = \left| \frac{1}{ka} \left[sin(\frac{ka}{2} + kb) - sin\Big(\frac{3ka}{2} + kb\Big) \right] + \frac{sin(\frac{ka}{2})}{\frac{ka}{2}} \right|^2 \tag{49}$$

where a is the conductor width, b is the gap between the signal and ground conductors and L is the length as shown in Fig.14, and k is the wave number of the spin wave in [rad/µm]. Note that for different types of antennas, eq. (49) takes a different form.

6.2 Experimental Setup

The experimental setup (Fig.15) to measure PSWS is essentially the same setup as used for the FMR experiment described in Chapter 5.2 but with some adjustments and the implementation of the new sample holder.

The electromagnet with two pole pieces by GMW Associates is applied to generate the external static magnetic field, which is measured with a Hall probe stuck to the middle of one of the pole pieces.

The DUT consists of a YIG film of 97 nm thickness grown on 500 µm thick (111) Gallium Gadolinium Garnet (GGG) substrate and a pair of coupled microwave CPW transducers. It is placed on the new sample holder, which is described in detail in the next chapter.

Two picoprobes (by GGB INDUSTRIES INC), which can be precisely arranged to couple to the CPW transducers (with conductor width $a = 250$ nm, gap between the signal and ground conductors $b = 750$ nm and length $L = 100$ µm) by utilizing two XYZ-stages (by

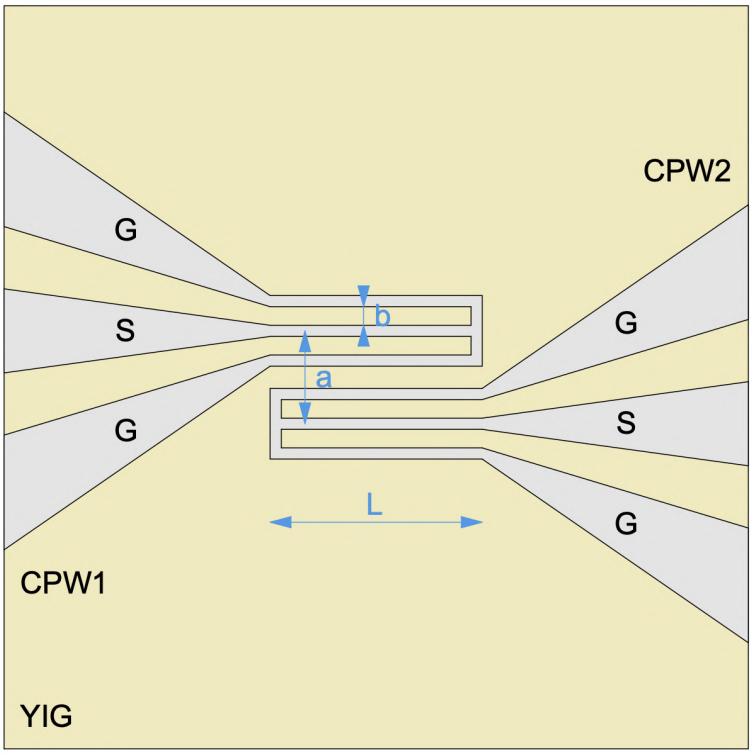

Figure 14: Schematic of the CPW transducers on YIG film with the conductor width $a = 250$ nm, the gap between the signal (S) and ground (G) conductors $b = 750$ nm and the length $L = 100$ µm is indicated. The center-to-center distance of the transducers is 3µm.

Thorlabs), are connected via high-frequency coaxial cables to the VNA (R & S, ZVA 40) to apply the microwave signal to the YIG film. An optical microscope is used to attach the picoprobes to the transducers.

6.3 New Setup for Out-of-plane Measurement

A significant part of the bachelor thesis entailed, improving the existing setup in the FMR-lab, by designing a new sample holder that would enable in-plane and additionally out-of-plane measurements.

At first, the complete existing setup for in-plane measurement was measured and then modeled in Inventor (see Fig.16 and Fig.17). The original setup consists of an aluminum stage with an affixed rail, an aluminum plate screwed onto a pair of wagons (DryLin'T by igus) that fit on the rail, two XYZ-stages by Thorlabs including two attached picoprobes (Model 40A by GGB INDUSTRIES INC) which themselves are screwed onto the plate. This setup allows the measurement of in-plane magnetization (DE and BV spin wave

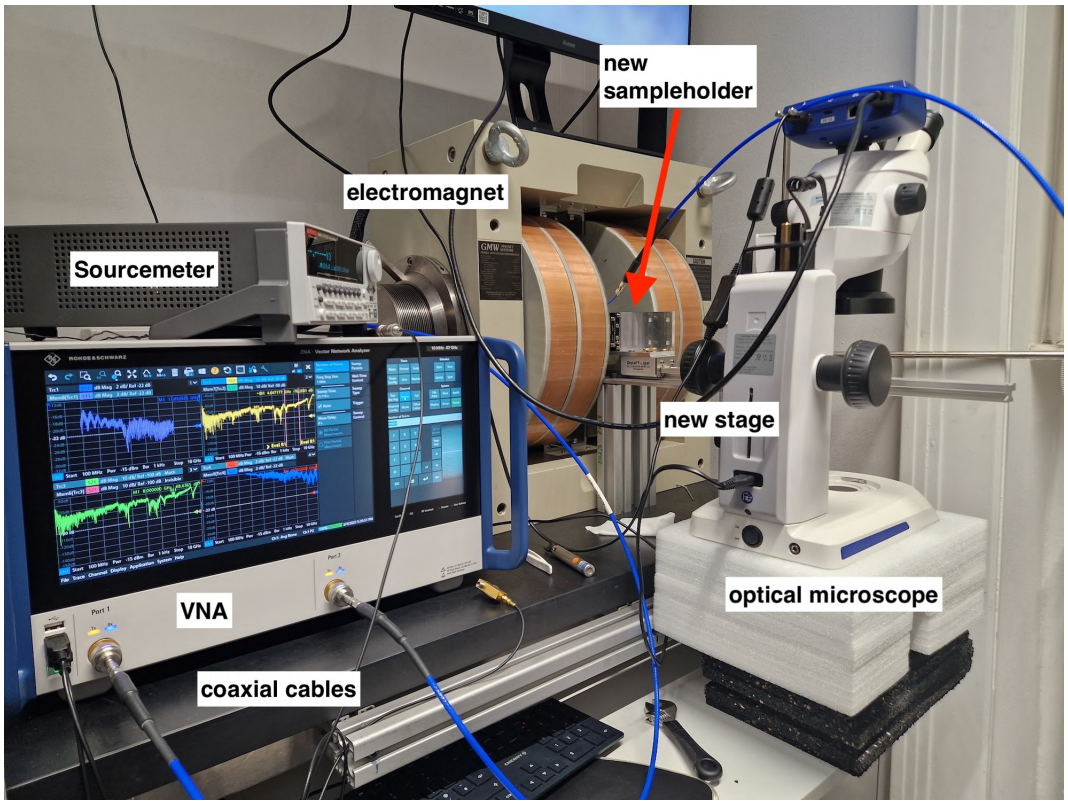

Figure 15: Experimental setup in the lab: electromagnet, VNA, sourcemeter, coaxial cables, optical microscope, new stage, and new sample holder.

modes) of samples.

To enable measurements of samples magnetized out-of-plane for FV modes, it was necessary to design a new sample holder including a new stage with an attached rail to place it on the table. Also two new XYZ-stages (Model PY005M by Thorlabs) with the additional ability of pitch and yaw adjustment were bought for this construction.

The new design (see Fig.18 and Fig.19) enables the placement of a sample or DUT on the sample holder and without having to remove the sample and the XYZ-stages including the attached picoprobes. The sample holder is then just rotated by 90° to switch between in-plane and out-of-plane placement inside of the electromagnets. Only the wagons have to be reattached on the other side. The optical microscope was also replaced with a new optical microscope with a flexible arm and better resolution, so the picoprobes can be connected correctly to the DUT in all configurations.

All the produced parts are made of aluminum and the screws are made of brass, which are non-magnetic materials as not to interfere with the measurement. The aluminum parts were produced at the workshop at the university.

An important consideration that particularly influenced the design of the new sample holder was the requirement for the sample to be positioned at the center of the magnetic pole pieces, ensuring a homogeneous magnetic field in both configurations. Another important aspect was the goal to approach the sample with the electromagnetic pole pieces as close as possible, which led to a narrower aluminum plate in the center. The placement of the XYZ-stages was designed to be outside the range of the pole pieces when in the in-plane position due to their width, which also defined the length of the holder. The dimensions of the construction were carefully specified to precisely accommodate the applied picoprobes and new XYZ-stages.

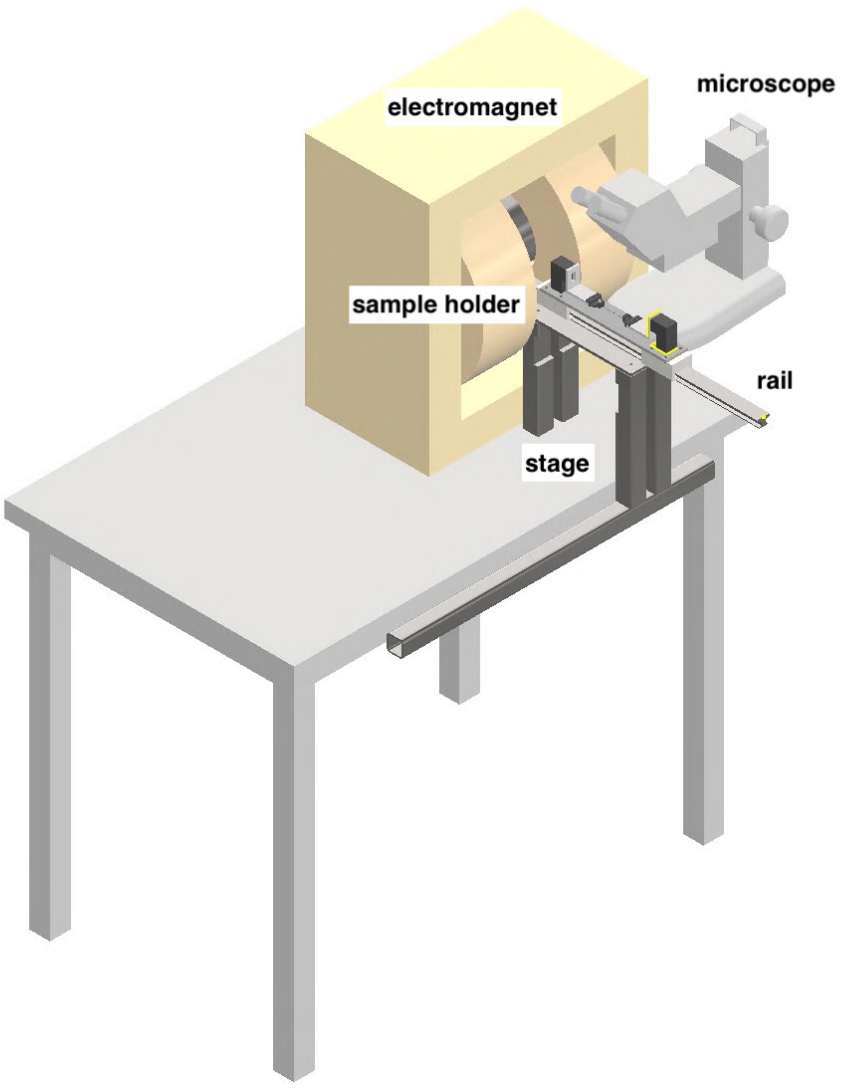

Figure 16: Existing experimental setup drawn with Inventor, pictured on the table with the electromagnets, microscope and the sample holder on the stage with the attached rail.

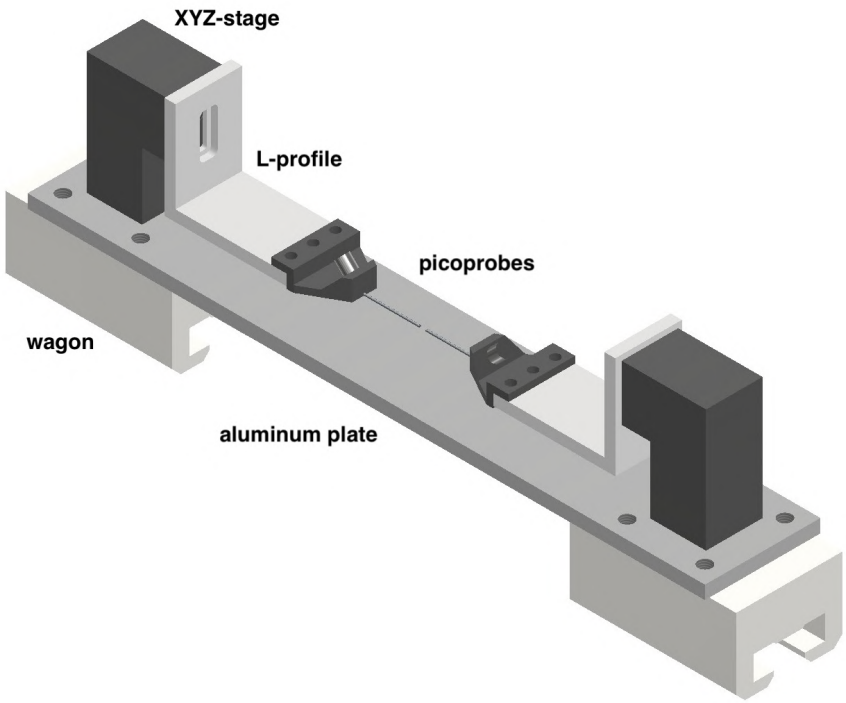

Figure 17: Original in-plane sample holder drawn with Inventor, pictured with the wagons, XYZ-stages and picoprobes attached via L-profiles.

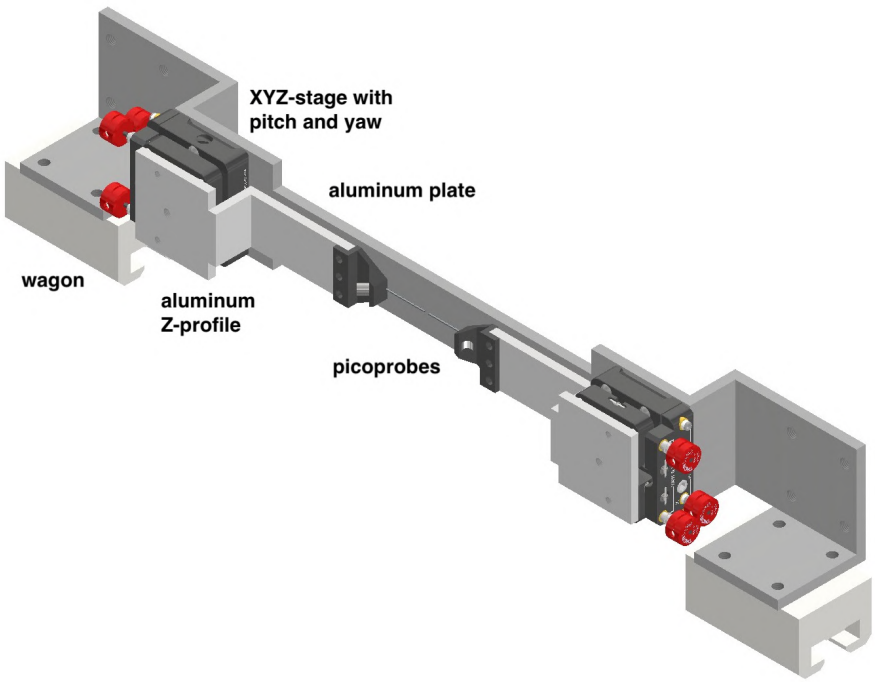

Figure 18: New experimental sample holder (XYZ-stages, picoprobes, wagons, aluminum plate and Z-profiles) in the out-of-plane configuration, drawn with Inventor.

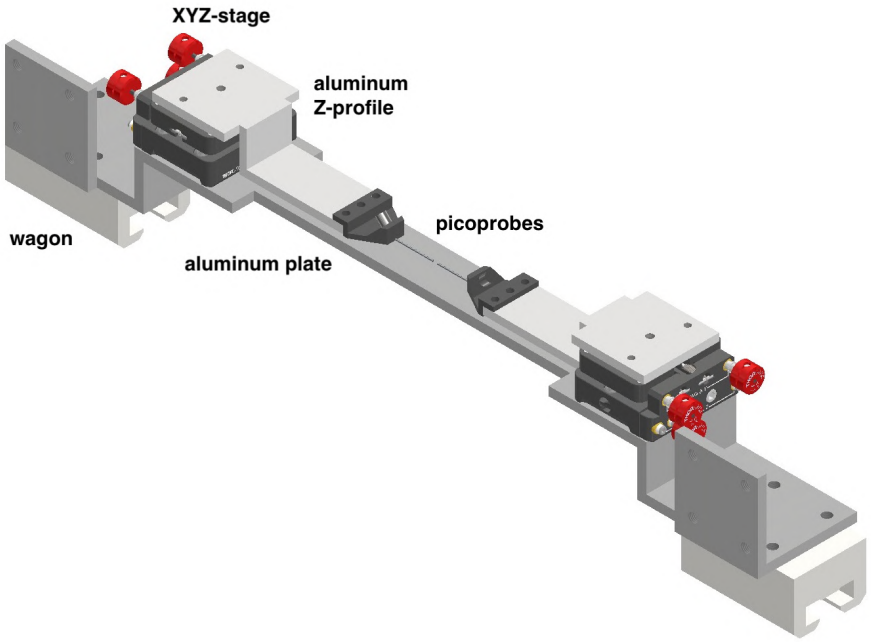

Figure 19: New experimental sample holder rotated by 90° for the in-plane configuration, drawn with Inventor.

Figure 20: New sample holder (XYZ-stages, picoprobes, wagons, aluminum plate, and Z-profiles and attached short flexible coaxial cables) with placed YIG sample in the out-of-plane configuration.

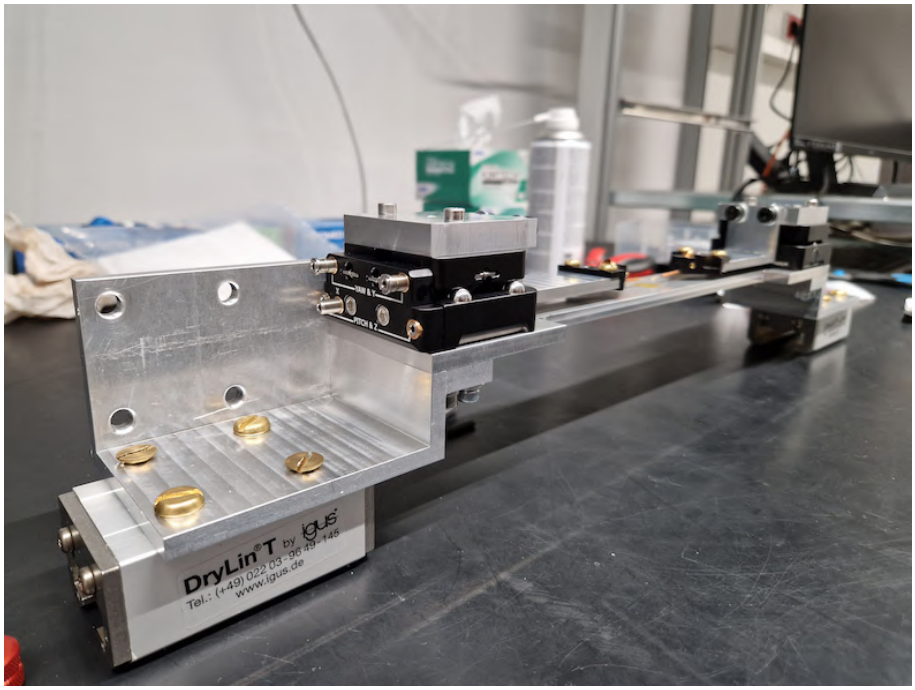

Figure 21: New sample holder (XYZ-stages, picoprobes, wagons, aluminum plate, and Z-profiles) in the in-plane configuration.

6.4 Measuring Process

Initially, the new sample holder was assembled. The DUT, consisting of a prepared YIG sample with the coupled pair of transducers, was mounted on the new sample holder for the in-plane and out-of-plane measurements. It turned out that the reach in the Z-direction of the new XYZ-stages was insufficient, so a glass slide with a height of approximately 1 mm was added beneath the YIG sample. Two flexible short coaxial cables were attached to the picoprobes. Next, the electromagnets were turned on with $B_{\text{ext}} = 0$ T. After sliding the sample holder onto the rail and attaching the longer coaxial cables, the picoprobes were carefully attached to the transducers using the XYZ-stages and the optical microscope. The unique shape of the CPW transducers, as shown in Fig.22 (b), was designed to enable the measurement of both in-plane modes (DE and BV) by simply rotating the sample on the sample holder, as the picoprobes themselves cannot be rotated.

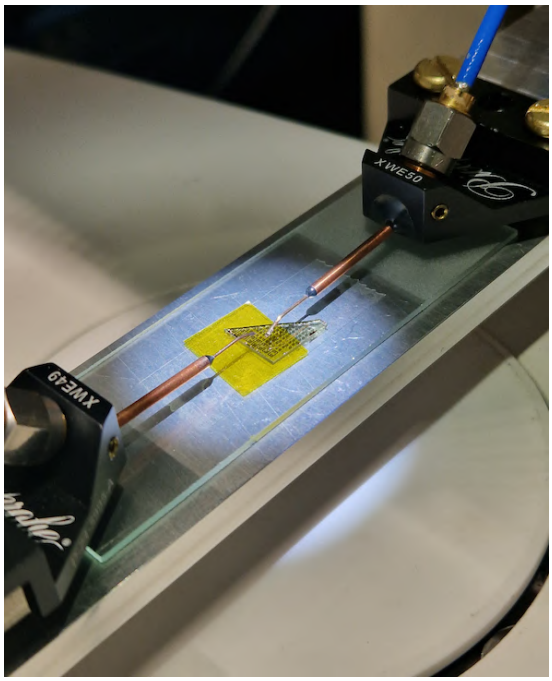

(a) Detailed photo of the placed YIG sample on the glass slide on the new sample holder with attached picoprobes.

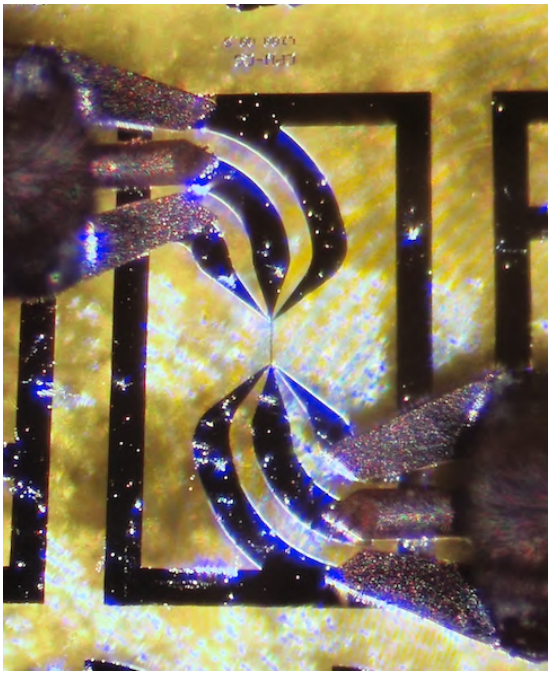

(b) Enlarged microscopic picture of the YIG sample and the specially shaped CPW transducers and the attached sensors of the picoprobes for the DE mode.

Figure 22: Detailed photos of the placed and attached YIG sample.

To verify the connection of the picoprobes, the ohmmeter mode of the sourcemeter was used. Finally, after slowly sliding the sample holder in until the YIG sample was in the

middle of the two electromagnet pole pieces, the coaxial cables were connected to the VNA. The calibration of the VNA was not necessary because a reference measurement was subtracted from the results.

The VNA was set up with an input power of -15 dBm which corresponds to 0.032 mW (dBm is an absolute value and not a ratio and means dB per 1 mW and can be easily converted with online calculators, for example on this website [25]), a bandwidth of 1 kHz, no averaging and single sweeps. Next, the VNA was used to apply varied frequencies around the expected frequency peak for the given external magnetic field.

To obtain more precise peak positions for the frequencies, corresponding to the employed magnetic field, the Kittel equation (eq.(18)) for a thin film magnetized in-plane was evaluated. This is because FMR represents the beginning of the signal peak for the propagating spin waves.

For each configuration (DE, BV, FV), frequency sweeps for several different values of the external magnetic field B_{ext} were measured, along with the reference signal $S_{12,\text{ref}}$ at $B_{\text{ext}} = 0$ T for each configuration.

The magnetic pole pieces could have been positioned closer to the sample for more precise results. However, since the primary goal of the experiment was to test the practicability of the new sample holder, this adjustment was not made, probably increasing the background noise.

As already mentioned, among the four S-parameters, only the transmission parameter S_{12} was considered for the evaluation, including both its real and imaginary parts. The resulting data points of each magnetic field value were saved for further evaluation.

The following values of the external magnetic field B_{ext} were measured:

- **DE mode** (sweep range: $(2-10)$ GHz with 1 MHz step size): 0 mT (reference), 50 mT, 100 mT, 150 mT, 200 mT, 250 mT, 300 mT

- **BV mode** (sweep range: $(2-10)$ GHz with 1 MHz step size): 0 mT (reference), 100 mT, 150 mT, 200 mT, 250 mT, 300 mT

- **FV mode** (sweep range: $(0.5-10)$ GHz with 100 MHz step size): 0 mT (reference), 50 mT, 100 mT, 150 mT, 200 mT, 250 mT, 300 mT, 350 mT

6.5 Results

The measurements for the DE, BV, and FV modes were processed and plotted using MATLAB.

In Fig.23, the measurements for each mode (BV, DE, FV) at different external magnetic field values B_{ext} are combined. This allows us to observe how the spin wave transmission peaks shift with increased magnetic fields in accordance with the predicted dispersion relations.

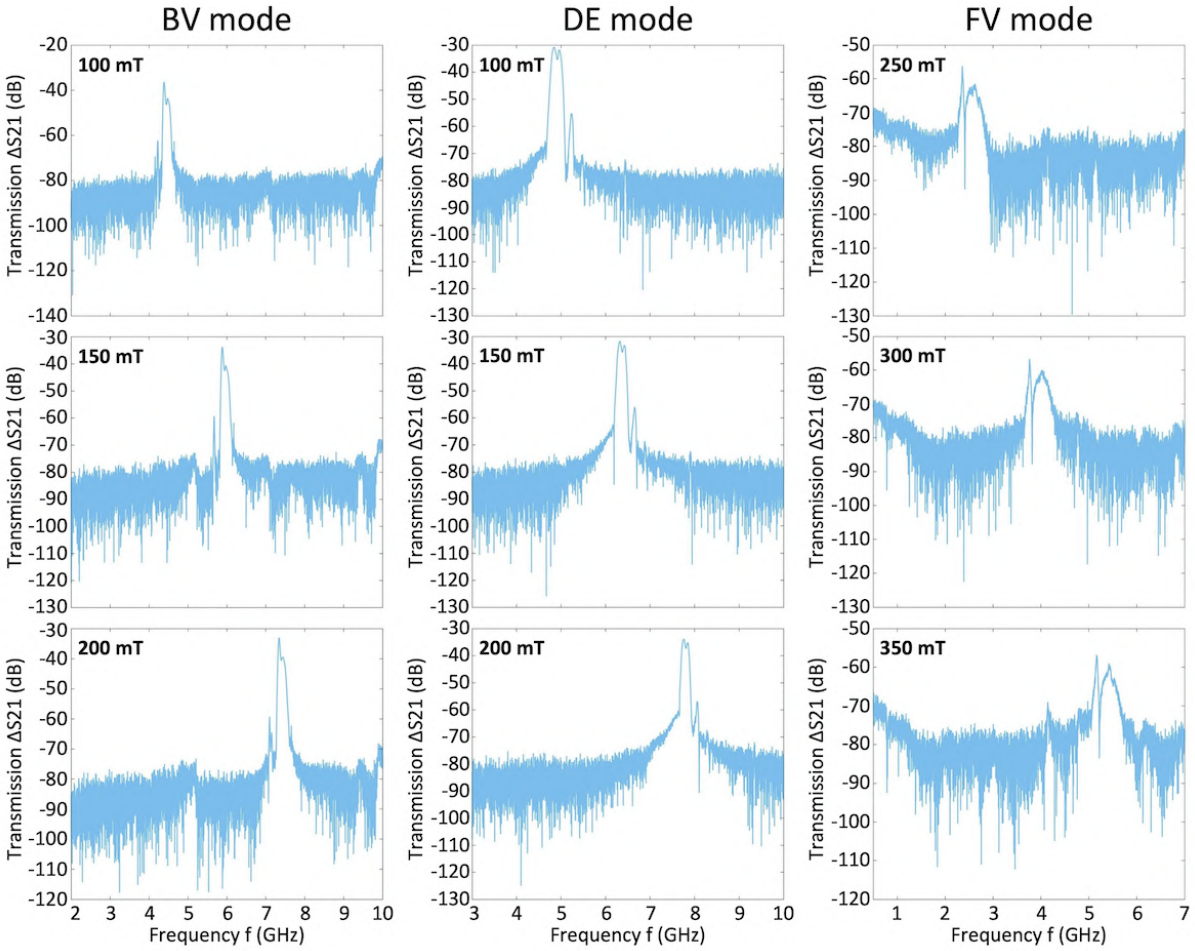

Figure 23: The measurements of the different modes are arranged in columns to show that the spin wave transmission peaks shift with increasing magnetic field as expected from the dispersion relation. From top to bottom, the magnetic field values B_{ext} are as follows: BV mode at: 100 mT, 150 mT, 200 mT; DE mode at: 100 mT, 150 mT, 200 mT; FV mode at: 250 mT, 300 mT, 350 mT.

An important fact is, the spin waves are only excited at the intersections of the dispersion relation and the peaks transducer excitation efficiency. For this reason, the measurements

of the DE, BV, and FV modes, along with their corresponding dispersion relations and transducer excitation efficiencies, were plotted for each mode to analyze their correlation.

The results are shown in Fig.24 for each mode (BV, DE, and FV): the graphs on the left show the ΔS_{12} (dB) spin wave spectrum as a function of the frequency (GHz). The graphs on the right show the dispersion relation, wave vector k (rad/µm) over the frequency (GHz) and the excitation efficiency J_{exc} over the frequency (GHz).

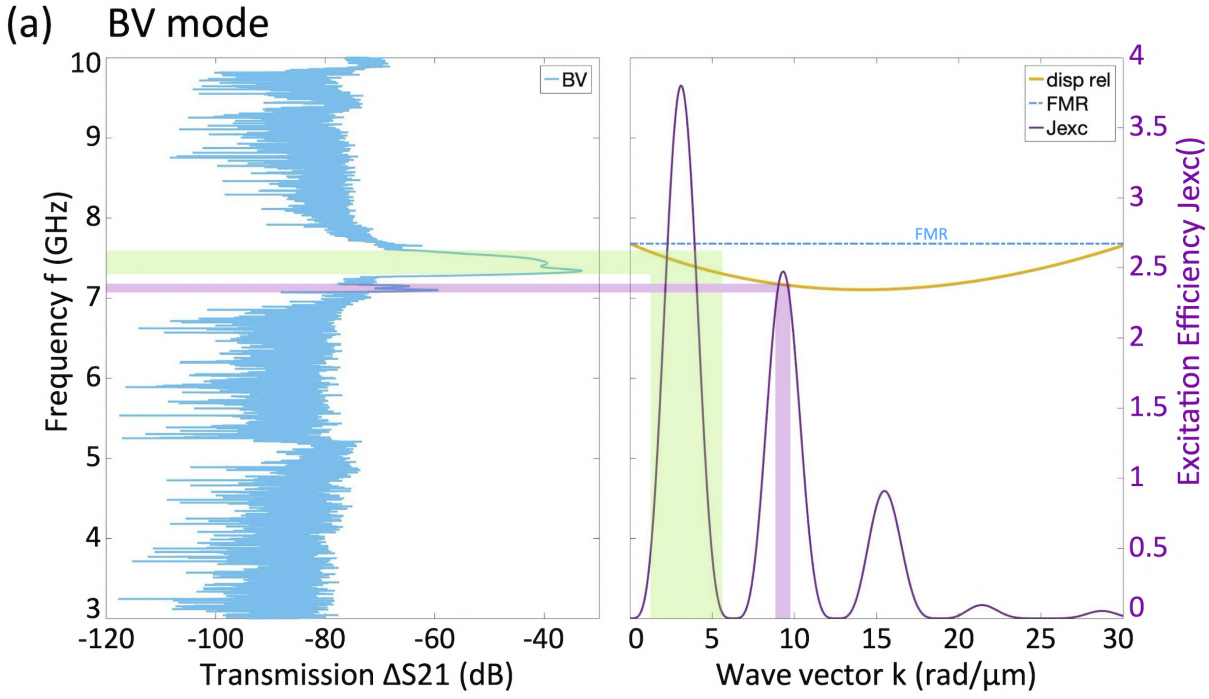

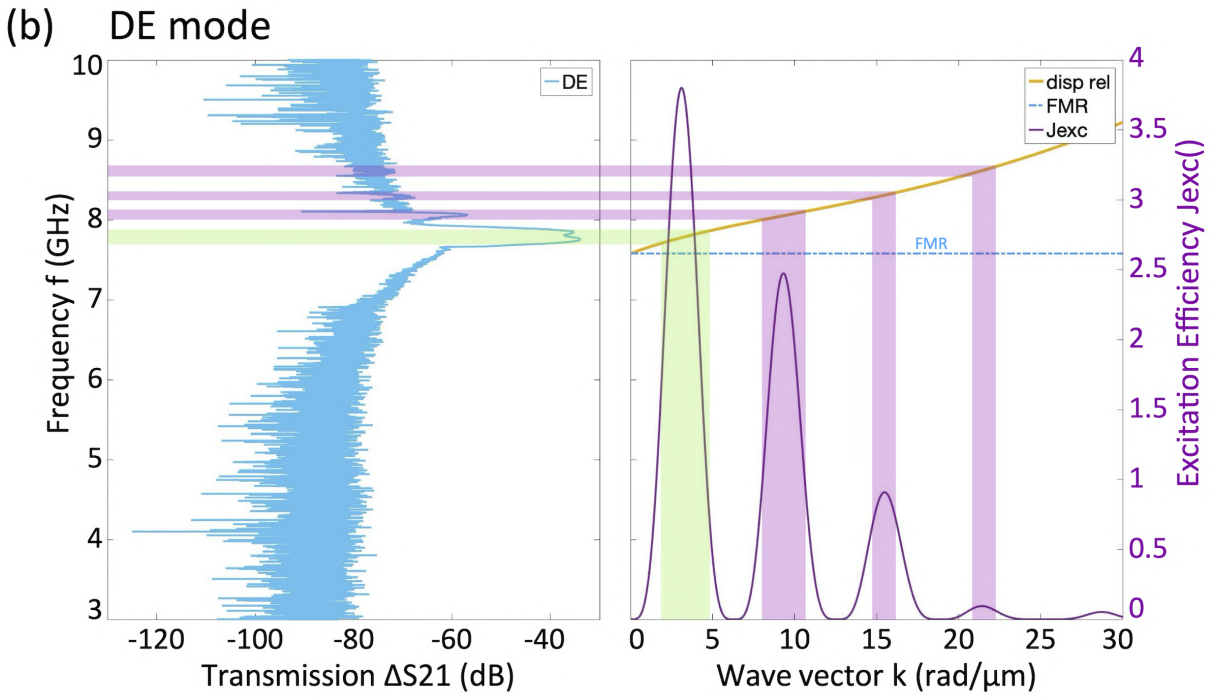

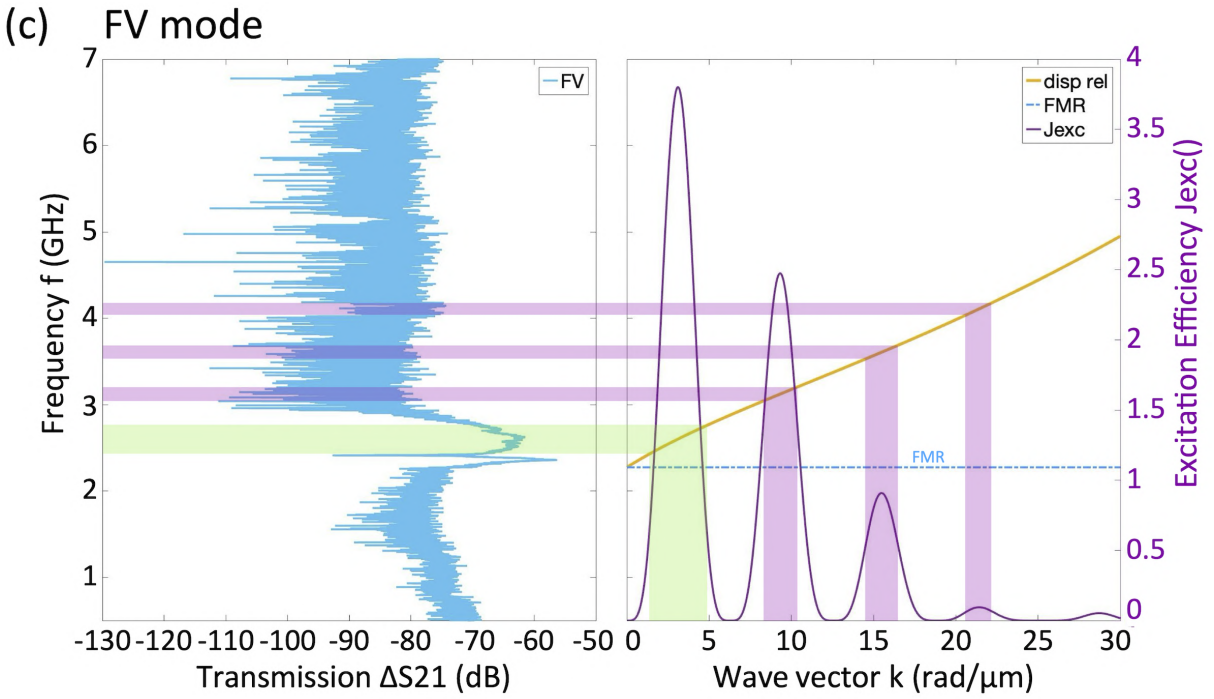

Figure 24: The peaks of the corrected spin wave transmission ΔS_{12} (blue) for (a) BV, (b) DE, and (c) FV modes are correlated with the intersection of the dispersion relation (yellow curve) and the transducer excitation efficiency J_{exc} (purple curve). The green highlights mark the first peaks of the correlation, while the purple highlights indicate additional peaks. The blue dashed line represents the FMR frequencies, showing the onset of spin wave excitation.

The peaks of the transmission S_{12} are correlated with intersections of the dispersion relation and the peaks of the transducer excitation spectrum for all modes and highlighted (first peak in green, additional peaks in purple).

While the correlations are not perfect, they could be improved with more meticulous conduct of the experiments. It is important to note, that the primary goal of the measurements was not to obtain perfect results, but rather to test the new sample holder. As such, the experiments were not conducted with the utmost precision. Specifically, the magnetic pole pieces were positioned relatively far from the sample for each mode. Since the Hall probe was attached to one of the pole pieces, the measured magnetic field was also farther from the sample than ideal, probably leading to a shift in the correlation of the peaks.

Additionally, the calculation of the transducer excitation efficiency J_{exc} in eq.(49) relied on an analytical Fourier transformation, assuming an infinitely thin transducer with a normalized current density, rather than the actual empirical dimensions. This probably also contributes to the peak displacement ([24]).

Concerning the FV geometry shown in Fig.24 (c), only two resonance peaks appear in the spin wave transmission spectrum: the uniform FMR mode (PSSW with totally unpinned boundary condition: n= 0), which simultaneously marks the onset of spin wave excitation, and the first thickness PSSW mode (n= 1) (see Chapter 2.4). Higher-order PSSW modes (n$\geq$ 2) are not observed.

The absence of the higher-order standing modes can be understood by examining the spatial profile of the applied microwave magnetic field (also referred to as radio frequency (RF) field) $b_{\mathrm{ext}}(t)$ within the CPW. The wave vectors k of the excited spin waves can be calculated by the Fourier transform of the spatial distribution of the RF field. This field can be decomposed into two spatial components: the horizontal (or IP) component, parallel to the wave vector k, and the perpendicular (or OOP) component, perpendicular to k. In the BV configuration, only the OOP component contributes to the excitation of spin waves, since the IP component is parallel to the applied magnetic field B_{ext} and thus can be neglected. In the DE configuration, both spatial components contribute to spin wave excitation because they are both perpendicular to the bias field B_{ext}, enhancing antenna excitation efficiency. And in the FV configuration, mainly the IP component excites spin waves, which in this case is perpendicular to the bias field B_{ext}, if this field is

strong enough so the OOP component of the RF field can be neglected.

Although the IP component of the RF field is responsible for the spin dynamics in both DE and FV geometries, the spatial distribution of this component differs between the two configurations. In FV configurations, the spin waves are propagating nearly uniformly over the CPW width, unlike in the DE configuration. Thus, the Fourier transform of the RF field within the CPW has a sharp maximum peak at $k = 0$, with a rapid decay for the wave vectors associated with higher-order modes. As a result, the (n$\geq$ 2) modes are not efficiently excited and, consequently, do not appear in the measurement [17], [26].

6.6 Discussion and Analysis

The new sample holder fits well within the experimental setup and was successfully tested in the PSWS configurations. However, the new pair of XYZ-stages proved somewhat inconvenient due to their limited movement range of only 3 mm in the XYZ-directions. To compensate for this limitation, modifications such as adding a glass slide beneath the sample were necessary. Moreover, the XYZ-stages exhibit additional movements caused by their pitch and yaw abilities, which further complicate positioning and make correct adjustments even more difficult.

For future improvements, several optimizations can be made. For example, rotating the XYZ-stages by 90 degrees could enhance accessibility, as some adjustments require a hexagonal wrench due to the supplied buttons not fitting properly.

Another potential improvement is combining the original XYZ-stages with the new ones to extend the XYZ-movement range while adding yaw and pitch control. However, feasibility needs to be assessed, as this adaptation would require a longer sample holder. Furthermore, the combined stages might not even fit through the magnets when positioned at their maximum separation.

The data collected for the new sample holder provides a valuable foundation for designing an improved model, incorporating the insights gained from this experiment.

7 Conclusion

In the frame of this thesis, a fundamental understanding of magnetization dynamics, spin waves, magnonics, and relevant research techniques was developed. Beyond the theoretical foundation, the primary focus was on designing and developing a new sample holder for the existing experimental setup in the FMR laboratory at the University of Vienna. This process also provided valuable insights into the functionality of the setup and deepened the understanding of the applied measurement techniques.

The newly developed sample holder significantly enhances the experimental capabilities by enabling the measurement of additional spin wave modes. Previously, the original setup only allowed the study of DE and BV spin wave modes; with the newly developed sample holder, FV mode measurements are now also accessible.

Furthermore, experiments were conducted to deepen the understanding of the measurement techniques and also validate the functionality of the new sample holder. FMR measurements were performed using the original setup, while PSWS experiments were conducted with the newly developed sample holder. The successful demonstration of its performance confirms its potential to facilitate future spin wave research and enhance experimental possibilities in the field of magnonics.

The results of this thesis are particularly relevant for researchers exploring spin wave excitation and propagation mechanisms, as the expanded measurement capabilities provide new possibilities in experimental procedure. The successful demonstration of its performance confirms its ability to extend the range of spin wave measurements within this specific setup, making it a valuable addition to ongoing research in magnonics.

However, some limitations were identified: the dimensions of the sample holder are specifically tailored to the chosen XYZ-stages and picoprobes, meaning modifications may be necessary if different components are required. Additionally, the new XYZ-stages proved to be somewhat inconvenient, highlighting an opportunity for improvement in a future sample holder design.

This work establishes a foundation for further spin wave investigations and offers a pathway for refining experimental hardware to enhance measurement capabilities. Future developments may focus on refining the sample holder's design to enhance its adaptability and ease of use while maintaining its ability to support a broad range of spin wave measurements.

List of Abbreviations

BV	Backward Volume Magnetostatic Spin Waves
BW	Bandwidth
CPW	Coplanar waveguide
DE	Damon-Eshbach Magnetostatic Spin Waves
DUT	Device under Test
FMR	Ferromagnetic Resonance
FWHM	Full Width at Half Maximum
FV	Forward Volume Magnetostatic Spin Waves
GGG	Gallium Gadolinium Garnet
IP	In-plane
LL-eq.	Landau-Lifshitz equation
LLG-eq.	Landau-Lifshitz-Gilbert equation
MSSW	Magnetostatic Surface Spin Waves
OOP	Out-of-plane
PSSW	Perpendicular Standing Spin Waves
PSWS	Propagating Spin Wave Spectroscopy
RF	Radio Frequency
S-Parameters	Scattering Parameters
VNA	Vector Network Analyzer
YIG	Yttrium-Iron-Garnet

References

[1] A. Chumak, A. Serga, and B. Hillebrands, "Magnonic crystals for data processing," *Journal of Physics D: Applied Physics*, vol. 50, no. 24, p. 244 001, May 2017. DOI: 10.1088/1361-6463/aa6a65. [Online]. Available: https://dx.doi.org/10.1088/1361-6463/aa6a65.

[2] A. V. Chumak, V. I. Vasyuchka, A. A. Serga, and B. Hillebrands, "Magnon spintronics," *Nature Physics*, vol. 11, no. 6, pp. 453–461, Jun. 2015, ISSN: 1745-2481. DOI: 10.1038/nphys3347. [Online]. Available: https://doi.org/10.1038/nphys3347.

[3] A. J. Princep, R. A. Ewings, S. Ward, *et al.*, "The full magnon spectrum of Yttrium Iron Garnet," *npj Quantum Materials*, vol. 2, no. 1, Nov. 2017, ISSN: 2397-4648. DOI: 10.1038/s41535-017-0067-y. [Online]. Available: http://dx.doi.org/10.1038/s41535-017-0067-y.

[4] K. M. Krishnan, *Fundamentals and Applications of Magnetic Materials*, 8th. Oxford University Press, 2016, ISBN: 9780199570447.

[5] D. D. Stancil and A. Prabhakar, *Spin Waves - Theory and Applications*. Springer New York, NY, 2009, ISBN: 978-0-387-77865-5. DOI: 10.1007/978-0-387-77865-5.

[6] J. M. D. Coey, *Magnetism and Magnetic Materials*. Cambridge University Press, 2009, ISBN: 9780521816144.

[7] A. V. Gurevich and V. V. Melkov, *Magnetization Oscillations and Waves*. Boca Raton, FL: CRC Press, 1996, ISBN: 9780849394607.

[8] C. Kittel, "On the theory of ferromagnetic resonance absorption," *Phys. Rev.*, vol. 73, pp. 155–161, 2 Jan. 1948. DOI: 10.1103/PhysRev.73.155. [Online]. Available: https://link.aps.org/doi/10.1103/PhysRev.73.155.

[9] M. P. RPTU, accessed: 19.02.2025. [Online]. Available: https://mandmems.eu/spin-waves/.

[10] B. Kalinikos and A. Slavin, "Theory of dipole-exchange spin wave spectrum for ferromagnetic films with mixed exchange boundary conditions," *Journal of Physics C: Solid State Physics*, vol. 19, no. 35, pp. 7013–7033, Dec. 1986. DOI: 10.1088/0022-3719/19/35/014. [Online]. Available: https://iopscience.iop.org/article/10.1088/0022-3719/19/35/014.

[11] D. J. Griffiths and D. F. Schroeter, *Introduction to quantum mechanics*, Third edition. Cambridge ; New York, NY: Cambridge University Press, 2018, ISBN: 9781107189638. DOI: 10.1017/9781316995433.

[12] Wikipedia, *Group velocity*, accessed: 08.01.2025. [Online]. Available: https://en.wikipedia.org/wiki/Group_velocity.

[13] B. Hillebrands, *Introduction to spintronics – Ring Lecture SS2024*, Lecture notes, RPTU Kaiserslautern-Landau, April 25, 2024. [Online]. Available: https://physik.rptu.de/fileadmin/hillebrands/Lehre/SS24/2024.04.25_Hillebrands_-_Ringvorlesung_SS2024.pdf.

[14] B. Samantaray, A. Singh, C. Banerjee, A. Barman, P. Alagarsamy, and P. Mandal, "Perpendicular standing spin wave and magnetic anisotropic study on amorphous FeTaC films," *IEEE Transactions on Magnetics*, vol. 52, pp. 1–4, Jan. 2016. DOI: 10.1109/TMAG.2016.2520981.

[15] P. Gruszecki, C. Banerjee, M. Mruczkiewicz, O. Hellwig, A. Barman, and M. Krawczyk, "Chapter two - the influence of the internal domain wall structure on spin wave band structure in periodic magnetic stripe domain patterns," in *Recent Advances in Topological Ferroics and their Dynamics*, ser. Solid State Physics, R. L. Stamps and H. Schultheiß, Eds., vol. 70, Academic Press, 2019, pp. 79–132. DOI: https://doi.org/10.1016/bs.ssp.2019.09.003. [Online]. Available: https://www.sciencedirect.com/science/article/pii/S0081194719300037.

[16] H. J. Waring, Y. Li, N. A. B. Johansson, C. Moutafis, I. J. Vera-Marun, and T. Thomson, "Exchange stiffness constant determination using multiple-mode FMR perpendicular standing spin waves," *J. Appl. Phys.*, vol. 133, no. 6, p. 063 901, 2023. DOI: 10.1063/5.0135024.

[17] A. A. Serga, A. V. Chumak, and B. Hillebrands, "YIG magnonics," *J. Phys. D: Appl. Phys.*, vol. 43, p. 264 002, 2010. DOI: 10.1088/0022-3727/43/26/264002.

[18] K. Davídková, "Master thesis: Nonlinear spin-wave power limiter for RF applications," M.S. thesis, Brno, 2023.

[19] I. TEKTRONIX, *VNA Primer*. [Online]. Available: https://www.tek.com/en/documents/primer/what-vector-network-analyzer-and-how-does-it-work.

[20] F. Caspers, "RF engineering basic concepts: S-parameters," *Scientific Information Service CERN*, pp. 67–93, 2012. DOI: 10.48550/arXiv.1201.2346. arXiv: 1201.2346 [physics.acc-ph]. [Online]. Available: https://cds.cern.ch/record/1415639/files/p67.pdf.

[21] G. Nyikayaramba and B. Murmann, "S-parameter-based defect localization for ultrasonic guided wave SHM," *Aerospace*, vol. 7, no. 3, p. 33, 2020, ISSN: 2226-4310. DOI: 10.3390/aerospace7030033. [Online]. Available: https://www.mdpi.com/2226-4310/7/3/33.

[22] Z. Zhang and Y. Wei, "Optimization of experiment settings in ferromagnetic resonance measurements," *Results in Physics*, vol. 7, pp. 2614–2618, 2017, ISSN: 2211-3797. DOI: https://doi.org/10.1016/j.rinp.2017.06.056. [Online]. Available: https://www.sciencedirect.com/science/article/pii/S2211379717302814.

[23] P. Pirro, T. Brächer, A. V. Chumak, *et al.*, "Spin-wave excitation and propagation in microstructured waveguides of yttrium iron garnet/Pt bilayers," *Applied Physics Letters*, vol. 104, no. 1, Jan. 2014, ISSN: 1077-3118. DOI: 10.1063/1.4861343. [Online]. Available: http://dx.doi.org/10.1063/1.4861343.

[24] K. Davídková, *Nanoscaled spin-wave frequency selective limiter (FSL) for 5G technology*, Jan. 2025. DOI: 10.5281/zenodo.14644055. [Online]. Available: https://doi.org/10.5281/zenodo.14644055.

[25] GoPhotonics, *dBm to Milliwatts Conversion Calculator*. [Online]. Available: https://www.gophotonics.com/calculators/dbm-to-milliwatts-conversion-calculator.

[26] J. Chen, F. Heimbach, T. Liu, *et al.*, "Spin wave propagation in perpendicularly magnetized nm-thick yttrium iron garnet films," *J. Magn. Magn. Mater.*, vol. 450, pp. 3–6, Jun. 2018, Perspectives on magnon spintronics. DOI: 10.1016/j.jmmm.2017.04.045.

[27] J. M. D. Coey and S. S. P. Parkin, *Handbook of Magnetism and Magnetic Materials*. Springer Nature Switzerland AG, 2021, ISBN: 9783030632090. DOI: 10.1007/978-3-030-63210-6.

[28] H. Kronmüller and S. S. P. Parkin, Eds., *Handbook of Magnetism and Advanced Magnetic Materials*. Chichester, UK: John Wiley & Sons, 2007, ISBN: 9780470022184. DOI: 10.1002/9780470022184.

[29] S. Demokritov, Ed., *Spin Wave Confinement*, 1st. Singapore: Jenny Stanford Publishing, 2009, ch. D2, ISBN: 9780429066535. DOI: 10.1201/9780429066535.

[30] W. Bang, J. Lim, J. Trossman, C. Tsai, and J. B. Ketterson, "Propagation of magnetostatic spin waves in an Yttrium Iron Garnet film for out-of-plane magnetic fields," *Journal of Magnetism and Magnetic Materials*, vol. 456, pp. 241–250, 2018, ISSN: 0304-8853. DOI: 10.1016/j.jmmm.2018.02.030. [Online]. Available: https://www.sciencedirect.com/science/article/pii/S0304885317330895.

[31] T. E. Knowledge, accessed: 26.02.2025. [Online]. Available: https://www.theengineeringknowledge.com/s-parameters/.